14
Submicrometer-Scale Characterization of Solar Silicon by Raman Spectroscopy

Michael Becker, George Sarau, and Silke Christiansen

14.1
Introduction

Micro-Raman spectroscopy is a light scattering technique that has been used since several decades in solid-state sciences to investigate orientations of crystals, mechanical stresses, phase changes, and dopant concentrations in semiconductor materials [1–4]. Micro-Raman spectroscopy measures these and many other material properties via an inelastic interaction of laser light with lattice vibrations (mostly optical phonons). The method probes the material of interest nondestructively without requiring any complex sample preparations. Another beneficial aspect of micro-Raman spectroscopy is that, compared to many other methods, no expensive vacuum equipment is needed for the measurements. Micro-Raman spectroscopy allows for a lateral resolution of the order of at least $\sim$200 nm–1.5 μm (depending on the excitation wavelength) when focusing the incident light beam through an objective on the sample surface. In addition, Raman signals can be mapped, providing images of elastic stress/strain-, orientation-, and doping-level distributions and of many other physical parameters [5]. In this chapter, we explain how to use micro-Raman spectroscopy to map and display some important parameters of solar silicon, such as the spatial distribution of stress/strain, crystal grain orientations, and dopant-level distributions. We will present several qualitative maps of these parameters and describe in detail how to extract quantitative information from the respective images. Though the theoretical descriptions and calculation procedures to obtain quantitative information from Raman measurements are sometimes complicated and lengthy, often all necessary parameters can be obtained from one measurement cycle, and once the calculation procedures are implemented, the calculations can be carried out rather rapidly. This chapter starts with a description of the procedure to determine the crystal orientation of arbitrarily oriented silicon grains in polycrystalline solar cell wafers from Raman measurements. Once the crystal orientation is determined, a detailed analysis of the stress/strain states within the different grains becomes feasible. A detailed description of the physical background concerning the stress/strain state measurements in polycrystalline solar

Mechanical Stress on the Nanoscale: Simulation, Material Systems and Characterization Techniques, First Edition.
Edited by Margrit Hanbücken, Pierre Müller, and Ralf B. Wehrspohn.
© 2011 Wiley-VCH Verlag GmbH & Co. KGaA. Published 2011 by Wiley-VCH Verlag GmbH & Co. KGaA.

materials and some illustrative examples of stress/strain analysis will be presented in Section 14.3.

Highly doped regions in mono- or polycrystalline silicon solar cells, such as the emitter- or the back surface field (BSF) region, are essential for the proper and effective operation of solar cells. A highly n-doped layer (emitter) at the upper surface of a silicon solar cell is necessary to produce a p–n junction and a highly p-doped layer (BSF) of a few micrometer thickness is necessary to prevent the light-generated free carriers to recombine at the back surface of the solar cell. In Section 14.4, we describe a Raman-based method to determine the free carrier concentrations within these highly doped regions and to map their spatial distribution within silicon solar cells.

14.2 Crystal Orientation

14.2.1 Qualitative Maps

The measured Raman intensity of the threefold degenerate F_{2g} first-order Si Raman band depends on the Raman tensors, the scattering geometry during Raman measurements, for example, the polarization direction of the incident, and back-scattered light and on the respective crystal orientation (with reference to a fixed reference coordinate system). The Raman tensors $\boldsymbol{R}'_j$ [6] for the three (degenerate) Raman peaks are given below and correspond to a Si crystal whose axes are exactly aligned along the axes of the reference (sample stage) coordinate system (e.g., $x = x' = (100)$, $y = y' = (010)$, $z = z' = (001)$; see Figure 14.1 for descriptions):

$$\boldsymbol{R}'_x = \begin{pmatrix} 0 & 0 & 0 \\ 0 & 0 & d \\ 0 & d & 0 \end{pmatrix} \quad \boldsymbol{R}'_y = \begin{pmatrix} 0 & 0 & d \\ 0 & 0 & 0 \\ d & 0 & 0 \end{pmatrix} \quad \boldsymbol{R}'_z = \begin{pmatrix} 0 & d & 0 \\ d & 0 & 0 \\ 0 & 0 & 0 \end{pmatrix} \tag{14.1}$$

where d represents a material constant that is important only in case a comparison of the Si Raman peak intensities with the Raman peak intensities of other materials becomes necessary. Usually, d is set to 1. In the above-described case, the total measured Raman peak intensity is given by the simple approximation [7, 8]

$$I(\vec{e}_\mathrm{i}, \vec{e}_\mathrm{s}) \approx I_0 \cdot \sum_{j=1}^{3} \left| \vec{e}_\mathrm{i} \cdot R'_j \cdot \vec{e}_\mathrm{s} \right|^2 \tag{14.2}$$

$\vec{e}_i, \vec{e}_s$ are the polarization vectors of the incident and scattered light, respectively. The scaling parameter I_0 contains all fixed experimental parameters (laser intensity, wavelength, etc.). The index j discriminates the three phonon polarization directions x, y, and z and $\boldsymbol{R}'_j$ are the corresponding Raman tensors as given in Eq. (14.1). The approximation given above represents the Raman intensity–scattering geometry relationship rather well when an objective with a small numerical aperture (e.g., a $10x$ objective) is used to focus the laser spot on the sample surface (see Figure 14.1).

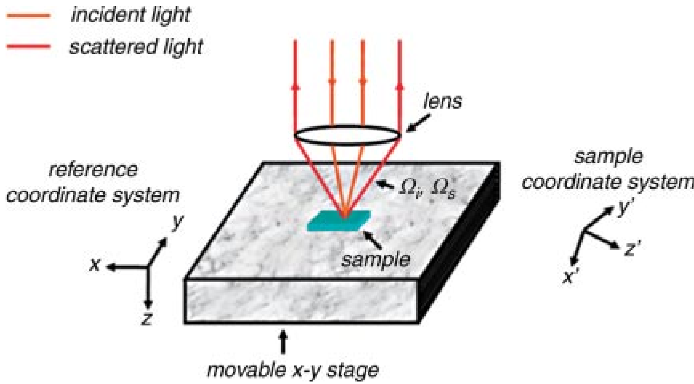

Figure 14.1 Schematic drawing of the sample stage of a micro-Raman spectroscopy setup. The incident laser beam is focused by a lens on the sample surface and the scattered light is collected by the same lens. Ω_i and Ω_s are the angles for the cones of the incident and scattered light, respectively, underneath the objective lens. The reference coordinate (stage) system remains fixed, whereas all physical properties of the sample (e.g., Raman tensors) refer to the sample (crystal) coordinate system.

Deviations from Eq. (14.2) occur when objectives with rather large numerical apertures are used. In this case, the strict polarization settings for the incident and backscattered beams are somewhat diluted by the continuous polarization directions within the cones of the incident and backscattered radiation under the objective. When evaluating qualitative orientation maps, these inaccuracies can be neglected. The three Raman tensors $\boldsymbol{R}'_j$ refer to the crystal coordinate system of the considered grain and have to be transformed to the reference coordinate system (sample stage) for arbitrary grain orientations, as the polarization directions $\vec{e}_\mathrm{i}$ and $\vec{e}_\mathrm{s}$ of the incident and scattered beams are defined in the stage coordinate system. The transformation into the reference coordinate system is accomplished by applying a rotation matrix $\boldsymbol{T}(\alpha, \beta, \gamma)$ to the Raman tensors $\boldsymbol{R}'_j$, where α, β, and γ represent the three Euler angles. The explicit expression for the rotation matrix $\boldsymbol{T}(\alpha, \beta, \gamma)$ can be found, for example, in Ref. [9]. By inserting the rotated Raman tensors $\boldsymbol{R}_j$ into Eq. (14.2), one obtains

$$I(\vec{e}_\mathrm{i}, \vec{e}_\mathrm{s}, \alpha, \beta, \gamma) \approx I_0 \sum_{j=1}^{3} \left| \vec{e}_\mathrm{i} \left(\boldsymbol{T}^{-1}(\alpha, \beta, \gamma) \boldsymbol{R'}_j \boldsymbol{T}(\alpha, \beta, \gamma) \right) \vec{e}_\mathrm{s} \right|^2 \qquad (14.3)$$

A qualitative map of crystal orientations within a certain region can now easily be achieved by fixed settings of the polarization directions of the incident and backscattered beams. The intensities of the Raman peaks then depend only on the components of the rotation matrix $\boldsymbol{T}(\alpha, \beta, \gamma)$ and therefore only on the specific crystal orientation. An example of such a qualitative orientation map is shown in Figure 14.2. Figure 14.2a displays an optical micrograph of a polycrystalline silicon wafer that is used for solar cells. After polishing and subsequent Secco etching [10], crystal defects such as dislocations and grain boundaries become visible. The grain sizes (areas) in this case vary from a few μm^2 to many hundred μm^2. Figure 14.2b represents the

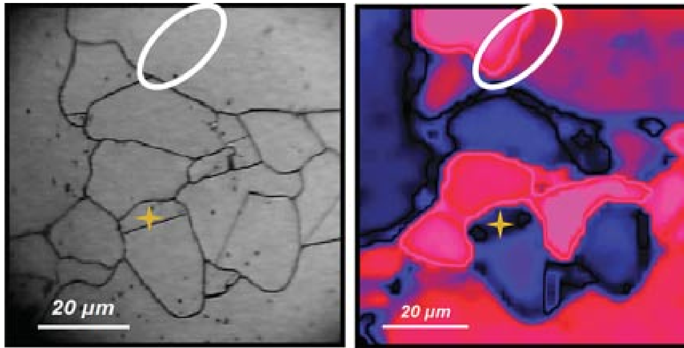

Figure 14.2 (a) Optical micrograph of a polycrystalline silicon solar cell wafer. The grain boundaries are made visible by Secco etching. (b) Qualitative map of the Raman intensities acquired within the same region. Blue/black color coding corresponds to high Raman intensities and red/purple to low intensities. The mapping shows that the Raman intensities can drastically change with different grain orientations, where the intensities follow the relation given in Eq. (14.3). The grain boundary within the white ellipse is visible only in the Raman intensity map, but not in the light optical micrograph.

intensities of the first-order silicon Raman peak. The intensities vary according to the relation given in Eq. (14.3), where $\vec{e}_{\mathrm{i}}$ and $\vec{e}_{\mathrm{s}}$ were both set to the y-position with respect to the stage system (in Porto notation [11] $z(y\,y)\bar{z}$, as the direction of the incident beam is along the z-axis of the stage system and the backscattered signal is collected along the negative z-axis).

The image of the Raman intensity map shown in Figure 14.2b reproduces very well the different grain orientations already visible due to the preferentially etched grain boundaries in the light optical micrograph (a). But it also reveals grain boundaries that are not visible in the optical micrograph (white ellipse). Therefore, crystal orientation imaging performed by micro-Raman spectroscopy provides more detailed and reliable information about the crystal orientation distribution than does a simple etching procedure.

14.2.2
Quantitative Analysis

A rather accurate quantitative determination of crystal orientation (we only discuss here the case of crystals with diamond structure, but the method discussed here can be easily adapted to other crystal structures) can be achieved when an objective with a small numerical aperture is used for the measurements of the Raman intensities. Equation (14.3) can then be used as a basis for quantitative orientation measurements by micro-Raman spectroscopy. The polarization direction $\vec{e}_{\mathrm{i}}$ of the incident laser beam is usually adjusted by a rotatable $\lambda/2$-plate (see Figure 14.3 for a detailed schematic drawing of the used Raman spectrometer setup and for the paths of the incident and backscattered light). Unfortunately, the influence of the mirrors and the notchfilter on the polarization direction of the incident beam after passing the

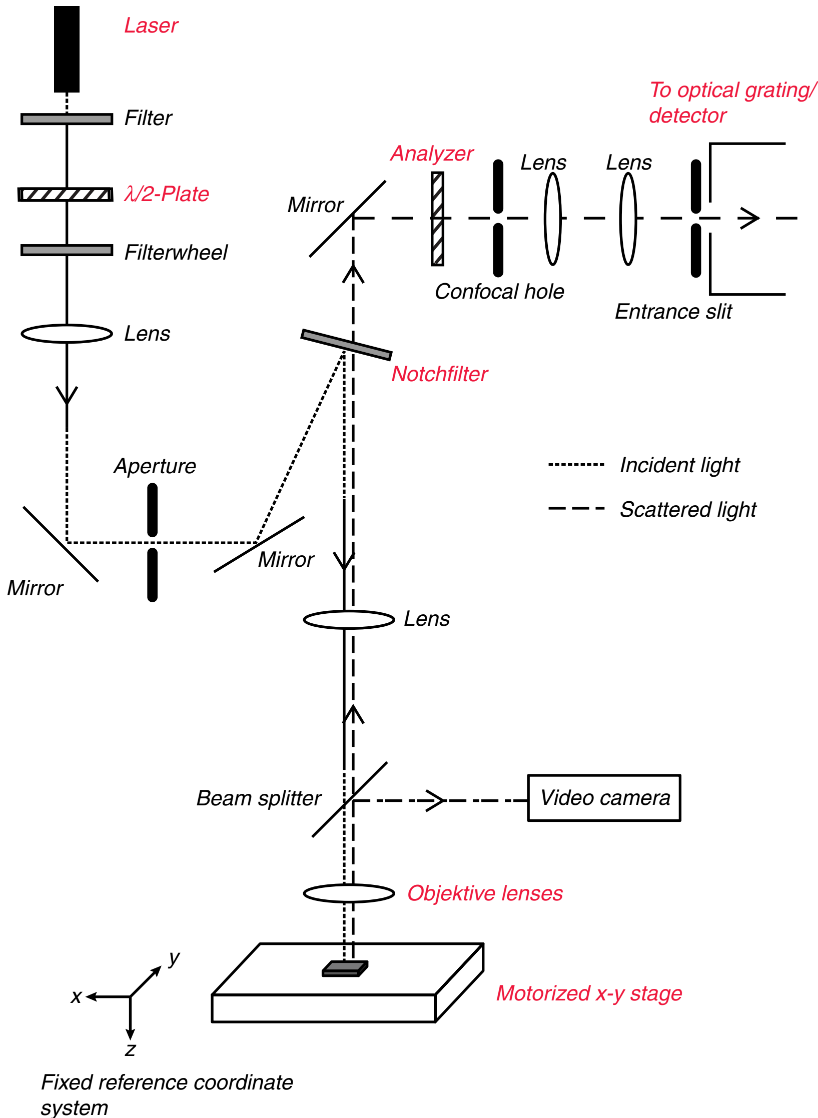

Figure 14.3 Detailed schematic drawing of the used Raman spectrometer setup (Jobin Yvon LabRam HR 800). With the rotatable $\lambda/2$-plate, the polarization direction of the incident beam can be adjusted continuously. With the analyzer in the backscattered path, the polarization direction of the backscattered signal is set. In contrast to the $\lambda/2$-plate, the analyzer can be set only to the *H* (horizontal) – or *V* (vertical) polarization direction with respect to the reference (sample stage) coordinate system (with a continuously adjustable $\lambda/2$-plate for the incident polarization direction, an additional continuously adjustable analyzer is not necessary).

$\lambda/2$-plate results in a dependence of the intensity of the incident laser beam on its polarization direction [9] and a difference in between the effective polarization direction ϕ on the sample surface and the original polarization direction $\tilde{\phi} = 2\theta$ that is adjusted with the $\lambda/2$-plate [9] (θ is the rotation angle of the $\lambda/2$-plate). These deviations can be accounted for by introducing a correction factor k, for example, the polarization vector of the incident beam is then elliptically dependent on the effective polarization direction ϕ at the sample surface $\vec{e}_\mathrm{i} = (\cos\phi, \quad k\sin\phi, \quad 0)^T$ with $0.9 \leq k \leq 1$ (usually)

As the optical grating of the spectrometer also affects the polarization dependence of the backscattered beam, the effective polarization vector $\vec{e}_\mathrm{s}$ of the scattered beam has to be modified according to $\vec{e}_\mathrm{s} = (m\cos\eta, \quad \sin\eta, \quad 0)^T \quad (m \approx 0.5)$. η describes the analyzer position ($\eta = 0°$ for analyzer in H-position, $\eta = 90°$ for analyzer in V-position). The correction factor m accounts for the optical grating to modify the polarization direction of the scattered beam. The influence of the optical grating could also be eliminated by putting a $\lambda/4$-plate (scrambler) into the path of the scattered light. As we will see, the influence of the grating is of no importance for the determination of crystallographic orientations. Therefore, we will not go into further details here. By using the expressions for the incident and backscattered polarization directions given above and Eq. (14.3), intensities of the orientation-dependent Raman peaks can be expressed through the following matrix equation:

$$I(\phi,\eta,\alpha,\beta,\gamma) \approx I_0 \cdot \begin{pmatrix} \cos^2\phi \\ k\cos\phi\sin\phi \\ k^2\sin^2\phi \end{pmatrix}^T \cdot \begin{pmatrix} f_{11} & f_{12} & f_{13} \\ f_{12} & f_{22} & f_{23} \\ f_{13} & f_{23} & f_{33} \end{pmatrix} \cdot \begin{pmatrix} m^2\cos^2\eta \\ m\cos\eta\sin\eta \\ \sin^2\eta \end{pmatrix} \qquad (14.4)$$

where the matrix functions $f_{ij} = f_{ij}(\alpha,\beta,\gamma)$ depend only on the three Euler angles α,β,γ. The explicit expressions for the functions f_{ij} are given in Ref. [12]. As there are only two possible analyzer positions (H and V), there are only two ϕ dependent functions left that are obtained from Eq. (14.4), $I_H(\phi) = I_0(f_{11}\cos^2\phi + \; kf_{12}\cos\phi\sin\phi + k^2f_{13}\sin^2\phi)m^2$ and $I_V(\phi) = I_0(f_{13}\cos^2\phi + kf_{23}\cos\phi\sin\phi + \; k^2f_{33}\sin^2\phi)$. Therefore, it is reasonable to fit the experimentally determined Raman peak intensity curves with the following two fit functions $F_H(\phi) = U_1\cos^2\phi + \; U_2\cos\phi\sin\phi + U_3\sin^2\phi$ and $F_V(\phi) = V_1\cos^2\phi + \; V_2\cos\phi\sin\phi + V_3\sin^2\phi$, where the factors U_1, V_1, and so on are the fitting parameters. By taking the four ratios of the fitting parameters $u_1 = U_1/U_3$, $u_2 = U_2/U_3$, $v_1 = V_1/V_3$, and $v_2 = V_2/V_3$ and comparing them with the corresponding ratios of the theoretical factors, one obtains a system of equations that is used to numerically determine the three Euler angles α,β,γ from the Raman intensity measurements:

$$\begin{aligned} &(k^2u_1)f_{13} - f_{11} = (ku_2)f_{13} - f_{12} = 0 \\ &(k^2v_1)f_{33} - f_{13} = (kv_2)f_{33} - f_{23} = 0 \end{aligned} \qquad (14.5)$$

The Euler angles are contained in the functions $f_{ij} = f_{ij}(\alpha,\beta,\gamma)$ (the correction factor m cancels in the equation system (14.5) and therefore the influence of the grating on the polarization direction of the backscattered Raman signal is eliminated).

Equation (14.5) represents an overdetermined system, as it contains four independent equations to calculate the three Euler angles α, β, γ. Therefore, an exact solution for the equation system (14.5) is not defined. Instead, the set of Euler angles has to be used that yields the minimal error belonging to the system (14.5). Once the Euler angles are determined, the whole information about the respective crystal orientation is known as the rotation matrix $\boldsymbol{T}(\alpha, \beta, \gamma)$ that can be easily recalculated from the Euler angles. As the rotation matrix $\boldsymbol{T}(\alpha, \beta, \gamma)$ can also be written in terms of the mutual angles in between the axes of the crystal and the axes of the reference (stage) system as

$$\boldsymbol{T} = \begin{pmatrix} \cos(\sphericalangle xx') & \cos(\sphericalangle xy') & \\ \cos(\sphericalangle yx') & \ddots & \\ & \cdots & \cos(\sphericalangle zz') \end{pmatrix}$$

the orientation of the respective crystal axes system with respect to the stage system can often be estimated at a glance. An experimental example measurement is shown in Figure 14.4, where the Raman peak intensity data are obtained from the grain marked in Figure 14.2 with a yellow asterisk. The measurement points are represented by the black squares and the blue dotted lines represent the best fit functions

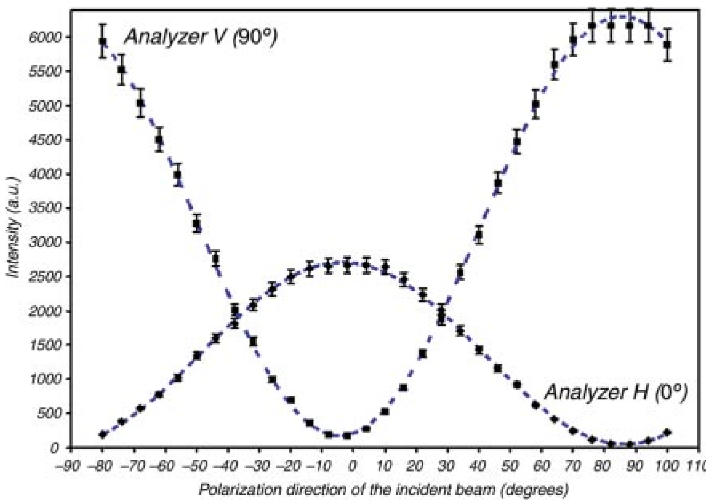

Figure 14.4 Variations of the Raman peak intensities with the polarization direction Φ of the incident beam, obtained from the grain marked with the yellow asterisk in Figure 14.3. The two curves belong to the two accessible analyzer positions (*H* and *V*). The black points represent the measurement data, whereas the blue dotted curves correspond to the respective best-fit functions $F_H(\phi)$ and $F_V(\phi)$ from which the three Euler angles α, β, γ and the rotation matrix $\boldsymbol{T}(\alpha, \beta, \gamma)$ are determined. The error bars account for the variations in the incident laser intensity with time. The maximum Raman peak intensities for the *H*- and *V*-analyzer positions are different due to the influence of the optical grating used for the spectral analysis (correction factor *m*). As explained in the text, this general difference in Raman intensities does not affect the determination of the crystal orientations.

$F_H(\phi)$ and $F_V(\phi)$ from which the three Euler angles α, β, γ, the rotation matrix $\boldsymbol{T}(\alpha, \beta, \gamma)$, and finally the values for $\cos(\sphericalangle xx')$ are determined.

From the experimental curves shown in Figure 14.4, we finally find the rotation matrix that contains the full information of the crystal orientation of the grain marked with the yellow asterisk in Figure 14.2

$$\boldsymbol{T}_{\text{Asterisk}} = \begin{pmatrix} 0.681 & -0.731 & 0.044 \\ 0.728 & 0.682 & 0.069 \\ -0.080 & -0.015 & 0.997 \end{pmatrix}$$

which shows that the angles $\sphericalangle xx'$, $\sphericalangle yy'$, and $\sphericalangle zz'$ are $\sim 47°$, $\sim 47°$, and $\sim 5°$, respectively, for example, a crystal that has its z'-axes almost exactly aligned along the z-axes of the stage coordinate system and where the x'- and y'-axes are rotated at an angle of $\sim 47°$ around the z-axes of the stage coordinate system.

14.2.3
Comparison with Other Orientation Measurement Methods

There are a few other competing methods to determine crystal orientations, each with certain advantages and drawbacks compared to the orientation measurements performed by micro-Raman spectroscopy. These are etching techniques [13–15], methods based on electron diffraction, such as transmission electron microscope (TEM) [16] or electron backscattering diffraction (EBSD) [17] and X-ray diffraction [18]. Etching techniques use selective etchants whose etching rates depend on the crystallographic orientation. The orientations of the remaining facets can then be determined by light reflection techniques. This technique needs no complicated equipment, but it is intrinsically destructive. In addition, this method lacks a good lateral resolution (a few tens of micrometers) and the determination of orientations is rather inaccurate. Much higher accuracy and better lateral resolution (few tens of nanometers) are achieved with electron diffraction (TEM, EBSD). However, prior to the measurements, the samples have to be destroyed because a thin foil has to be prepared for the TEM analysis or the sample surface needs special preparation when EBSD is used. Another drawback of these techniques is the expensive vacuum equipment. Less complex equipment is needed in the case of orientation determination by X-ray diffraction. Though the crystal orientations can be determined very accurately and the samples need not to be destroyed prior to the X-ray measurements, the lateral resolution lies only in the range of a few tens of micrometers, when standard instrumentation is used. Orientation measurements with micro-Raman spectroscopy do not need special sample preparation, as long as the surfaces are not too rough, which would lead to optical artifacts. Other important advantages of Raman spectroscopy are that the measurements can be performed under ambient conditions and within the range of a few hundred nanometers to a few micrometers (depending on the wavelength and the objective used), the lateral resolution is rather good. However, there are also a few drawbacks to the Raman spectroscopy-based orientation measurement method. One drawback lies in the measurement principle, which presumes that the material under investigation possesses at least one

Raman-active vibrational mode, for example, an optical phonon mode. This is usually not the case for most metals, as they possess only acoustic modes due to their simple crystal structure. These modes can be detected through Brillouin scattering [19], for example, inelastic light scattering of acoustic modes. However, Brillouin scattering experiments need more sensitive and intricate spectral detection techniques than what is usually used for Raman scattering experiments. Another drawback of orientation measurements with Raman spectroscopy is that they need several Raman intensity acquisitions for different positions of the $\lambda/2$-plate and the analyzer. As long as these optical devices cannot be adjusted automatically, their positions have to be adjusted by hand. In this case, orientation measurements become rather time consuming. The accuracy of the Raman spectroscopy-based orientation measurements lies at $\sim\pm 2^{\circ}$ for the determination of the Euler angles. Though this error value is sufficient for many other measurements that need the information about the crystal orientation (e.g., successive stress/strain measurements), the accuracy is far from the accuracy that can be achieved with X-ray diffraction. However, the great advantage of Raman spectroscopy-based orientation measurements is that subsequent Raman experiments that need the information about the crystal orientation can be performed in the same reference coordinate system. This would not be possible if other methods are used for orientation measurements.

14.3 Analysis of Stress and Strain States

14.3.1 General Theoretical Description

Mechanical stresses in crystals cause distortions of the crystal structure and a change in the average atomic distances. Changes in the crystal structure cause changes in the Raman tensors that finally result in modified Raman selection rules [20]. The modified average atomic distances cause shifts of the phonon eigenfrequencies. This effect can be described if one assumes that the components of the force constant matrix $\boldsymbol{K}$ depend on the average atomic distances and therefore on the stress/strain state within the specific crystal (i.e., deviations from the simple harmonic approximation are made) [21]. However, to calculate the strain-induced shift of phonon eigenfrequencies, a quasiharmonic approach is used [22]. That is, the components of the force constant matrix $\boldsymbol{K}$ are assumed to depend on the average atomic distances but stay independent of the atomic displacements during a lattice oscillation. The strain/stress-induced changes in the force constant matrix $\boldsymbol{K}$ can then simply be described by a perturbation matrix $\Delta\boldsymbol{K}$ [22–24]. Besides strain/stress in crystals, alloying crystals with foreign atoms leads also to a change in phonon eigenfrequencies. Analogous to the perturbation matrix $\Delta\boldsymbol{K}$, a second perturbation matrix $\Delta\boldsymbol{M}$ is introduced and added to the mass matrix $\boldsymbol{M}$ to describe the influence of the different masses of foreign atoms on the phonon frequencies. For further details see, for example, Refs [22, 25, 26]. The general eigenvalue problem to determine the phonon

frequencies in the presence of strain/stress and foreign atoms can then be written as [22]

$$[(\boldsymbol{K}+\Delta\boldsymbol{K})-\omega_r^2(\vec{q})\,(\boldsymbol{M}+\Delta\boldsymbol{M})]\,\vec{a}_r=0 \tag{14.6}$$

where $\omega_r(\vec{q})$ describes the eigenfrequency of a specific phonon mode r with wavevector $\vec{q}$. The corresponding eigenvector $\vec{a}_r$ describes the relative atomic displacements of atoms in an elementary cell of the crystal during a lattice oscillation (mode r). In the following, $\Delta\boldsymbol{M}=0$ is set as only the shifts of phonon frequencies due to strain/stress will be discussed here. For the force constant matrix $\boldsymbol{K}^{(\varepsilon')}=\boldsymbol{K}+\Delta\boldsymbol{K}$, usually a linear approach in the six independent strain tensor components $\varepsilon'=(\varepsilon'_{kl})\quad(k,l=x,y,z)$ [27] is used when stress/strain is present in the crystal [22] (prime quantities correspond to the crystal coordinate system). The components of the force constant matrix $\boldsymbol{K}^{(\varepsilon')}$ can then be expressed as

$$K_{ij}^{(\varepsilon')}=K_{ij}^0+\sum_{k,l}(\partial K_{ij}/\partial\varepsilon'_{kl})\varepsilon'_{kl}=K_{ij}^0+\sum_{k,l}K_{ijkl}^{(\varepsilon')}\varepsilon'_{kl} \tag{14.7}$$

with $K_{ij}^0=\omega_0^2\,\delta_{ij}$, where ω_0 is the phonon frequency of a certain mode without stress/strain. The components $K_{ijkl}^{(\varepsilon')}$ in Eq. (14.7) form a fourth-rank tensor and are called "phonon deformation potentials (PDPs)." The structure of this tensor and the number of its independent components are determined by the specific crystal symmetry. In case of crystals with cubic symmetry, the PDP-tensor contains only three independent components p, q, and r [23, 24, 28]. Phonon deformation potentials are material constants and can be determined by theoretical calculations [22] and measured experimentally [29, 30]. Solving the eigenvalue Eq. (14.6) with Eq. (14.7) and the three phonon deformation potentials p, q, and r for the three optical phonon modes of crystals with diamond structure (Si) leads finally to the following secular equation (for a detailed derivation see, for example, Refs [21, 22]):

$$\begin{vmatrix} p\varepsilon'_{xx}+q(\varepsilon'_{yy}+\varepsilon'_{zz})-\Delta\omega_r^2 & r\varepsilon'_{xy} & r\varepsilon'_{xz} \\ r\varepsilon'_{xy} & p\varepsilon'_{yy}+q\cdot(\varepsilon'_{xx}+\varepsilon'_{zz})-\Delta\omega_r^2 & r\varepsilon'_{yz} \\ r\varepsilon'_{xz} & r\varepsilon'_{yz} & p\varepsilon'_{zz}+q(\varepsilon'_{xx}+\varepsilon'_{yy})-\Delta\omega_r^2 \end{vmatrix}=0 \tag{14.8}$$

where $\Delta\omega_r^2=(\omega_r^2-\omega_{r0}^2)$ $(r=1,\ 2,\ 3)$ are the differences of the squared eigenfrequencies of the three phonon modes in the strained and unstrained state of the crystal. Using the approximation $\lambda_r=(\omega_r^2-\omega_{r0}^2)\approx 2\Delta\omega_{r0}\Delta\omega_r\Rightarrow\Delta\omega_r\approx\lambda_r/2\omega_{r0}$, the shifts in phonon frequencies $\Delta\omega_r$ can be easily determined from the eigenvalues λ_r. Using the secular Eq. (14.8), it is a rather simple task to determine the shifts of the phonon frequencies when the stress/strain state within the crystal is known. But for experimental applications, it is usually more preferable to determine the stress/strain states in crystals from the strain-induced shifts of the phonon frequencies. This is a more difficult task, as in the ideal case only three values of the frequency shifts are experimentally accessible at maximum. From these three experimental values, it is in principle not possible to determine all six strain or stress tensor components. In practice, some simplifying assumptions are made, concerning the strain/stress states, which lead to a reduction in the number of

tensor components that have to be calculated. The simplest Raman stress measurement scenario in case of silicon is a uniaxial stress state (only one nonzero stress tensor component) in a silicon wafer when the Raman signal is backscattered from the [001] surface. In this case, Eq. (14.8) leads to the rule of thumb, that a measured Raman peak shift of $\sim$1 cm^{-1} (wavenumbers) corresponds to a uniaxial stress of $\sim$500 MPa (see, for example, Refs [2, 31] for the numerical values of the PDPs and all other necessary material parameters). Though it has limited applicability in practice, this memorable relation can be used to estimate the stresses in more complex cases at a glance, for example, general stress states in arbitrarily oriented Si crystals.

14.3.2
Quantitative Strain/Stress Analysis in Polycrystalline Silicon Wafers

The determination of several stress tensor components in crystals with diamond structure with Raman spectroscopy has already been shown [32–36]. But the stress/strain analysis has been carried out only for monocrystalline samples with known orientation. Stress analysis in these cases is rather straightforward. Similar accurate stress tensor determination has not been accomplished for polycrystalline materials with diamond structure, for example, polycrystalline silicon wafers for solar cells or thin film transistors (TFTs) [37], due to the fact that grain orientation variations in these materials make stress measurements increasingly difficult. In this section, it will be demonstrated how several stress tensor components can be measured with micro-Raman spectroscopy in polycrystalline silicon within grains of arbitrary orientations. Examples of practical interest in the field of polycrystalline photovoltaic silicon material will be presented.

14.3.2.1 **Assumptions**

Equation (14.8) serves as the basis for determining the mechanical stress components also in polycrystalline silicon wafers. The strain tensor components, which occur in Eq. (14.8), refer to the specific crystal coordinate system (prime quantities). Also, all other physical properties of the crystal (e.g., phonon polarization directions) refer naturally to the respective crystal coordinate system. In polycrystalline wafers, a large number of crystallites with many different coordinate systems are present. Therefore, it is useful to refer the stress/strain states in the different crystallites to reference strain and stress tensors ε (strain) and σ (stress) that are defined in the fixed stage coordinate system (unprimed quantities). At the laser wavelengths (488 nm, 514 nm and 633 nm) used for the Raman measurements, the light penetrates only a few hundred nanometers to a few micrometers into weakly doped silicon [31] and only the stress/strain states close to the crystallite surface can be detected. The stress state directly at the crystallite surface is necessarily a planar stress state. Therefore, the reference stress tensor σ is chosen as follows:

$$\sigma = \begin{pmatrix} \sigma_{xx} & \tau_{xy} & 0 \\ \tau_{xy} & \sigma_{yy} & 0 \\ 0 & 0 & \Delta_z \end{pmatrix} \tag{14.9}$$

The additional component $\Delta_z(< \sigma_{xx}, \sigma_{yy})$ serves as a correction component that accounts for the slight deviations from the ideal planar stress state due to the finite penetration depth of the laser light.

14.3.2.2 **Numerical Determination of Stress Components**

The components of the reference stress tensor given in Eq. (14.9) can be determined from the experimentally three measured phonon frequency shifts $\Delta\omega_1$, $\Delta\omega_2$, and $\Delta\omega_3$ by using Eq. (14.8) according to the following procedure: The reference stress tensor (14.9) has to be transformed into the respective crystal coordinate system by using the rotation matrix $\boldsymbol{T}(\alpha, \beta, \gamma)$ (known from the orientation measurements). This gives the corresponding stress tensor $\sigma' = \boldsymbol{T}^{-1}(\alpha, \beta, \gamma)\sigma\boldsymbol{T}(\alpha, \beta, \gamma)$. The strain tensor components ε'_{kl} in Eq. (14.8) then have to be expressed in terms of the stress tensor components σ'_{kl} given above, through the inverse Hooke's law [38, 39] $\varepsilon' = \underline{\underline{\boldsymbol{S}}}\,\sigma'$, where $\underline{\underline{\boldsymbol{S}}}$ designates the elastic compliance tensor. As the strain and stress tensors are matrices, the compliance tensor $\underline{\underline{\boldsymbol{S}}}$ is consequently a fourth-rank tensor. However, as the strain and stress tensors are symmetric, the inverse Hooke's law can also be written in vector notation where the compliance tensor then becomes a 6×6 matrix. In case of cubic crystal structures (e.g., diamond and Si), the structure of the compliance tensor becomes rather simple and the number of independent components reduces to three. The values of these material constants for silicon (S_{11}, S_{12}, and S_{44}) can be found in literature [40]. The secular Eq. (14.8) can now be expressed in terms of the stress tensor components given in Eq. (14.9):

$$\left|\boldsymbol{A}\sigma_{xx} + \boldsymbol{B}\tau_{xy} + \boldsymbol{C}\sigma_{yy} + \boldsymbol{D}\Delta_z - \lambda_r \boldsymbol{E}\right| = 0 \tag{14.10}$$

where the components of the four symmetric 3×3 matrices $\boldsymbol{A}$, $\boldsymbol{B}$, $\boldsymbol{C}$, and $\boldsymbol{D}$ are simple but lengthy expressions [12] that depend on the elastic compliances S_{11}, S_{12}, S_{44}, on the phonon deformation potentials p,q,r, and on the components of the rotation matrix $\boldsymbol{T}(\alpha, \beta, \gamma)$. Therefore, the components of these four matrices are constants for a specific crystallite. $\boldsymbol{E}$ is the unit matrix. The "new" secular Eq. (14.10) leads to the characteristic polynomial $\boldsymbol{P}(\lambda_r) = \lambda_r^3 + \boldsymbol{a}\lambda_r^2 + \boldsymbol{b}\lambda_r + \boldsymbol{c}$, where the coefficients a, b, c are only functions of the stress components defined in Eq. (14.9). The roots of this polynomial correspond to the measured phonon frequency shifts $\lambda_r \approx 2\Delta\omega_{r0}\Delta\omega_r$. Comparing coefficients (rule of Vieta) finally leads to the equation system that is used to determine the stress components (14.9) numerically from the phonon frequency shifts:

$$\begin{aligned} a &= -2\omega_0(\Delta\omega_1 + \Delta\omega_2 + \Delta\omega_3) \\ b &= (2\omega_0)^2(\Delta\omega_1\Delta\omega_2 + \Delta\omega_1\Delta\omega_3 + \Delta\omega_2\Delta\omega_3) \\ c &= -(2\omega_0)^3(\Delta\omega_1\Delta\omega_2\Delta\omega_3) \end{aligned} \tag{14.11}$$

In practice, one uses the following way to calculate the stress components from the measured phonon frequency shifts: at first, an ideal planar stress state is assumed, that is, $\Delta_z = 0$ is set in Eq. (14.10). If then the numerical error of the system (14.11) is too large, Δ_z is used as a correction parameter and is iteratively adjusted to $\Delta_z \neq 0$ (in a reasonable range) until the numerical error corresponds to the minimal detectable

peak shift resolution of $\sim$0.05 cm^{-1} for all the three phonon frequency shifts $\Delta\omega_1$, $\Delta\omega_2$, and $\Delta\omega_3$.

14.3.3 Experimental Procedure to Determine Phonon Frequency Shifts

According to Eq. (14.11), all three phonon frequency shifts of the three optical phonons of silicon have to be measured experimentally to determine the components of the stress tensor. However, these three optical modes are always threefold degenerate in case of stress-free silicon. In case of stresses in the GPa range, the degeneracy is lifted enough and the three frequency shifts can be measured separately [41, 42] (but not in case of isotropic hydrostatic stress, as then the three phonon frequency shifts are the same [24]). In polycrystalline silicon wafers, the expected stress values are usually below 1 GPa and mechanical stresses of this magnitude cause phonon frequency shifts that are smaller than the experimentally measured half width of the main silicon Raman band. In this case, the lifting of degeneracy is not clearly visible and an accurate direct determination of the three frequency shifts $\Delta\omega_1$, $\Delta\omega_2$, and $\Delta\omega_3$ is not possible. However, by using three special polarization settings during the Raman measurements (incident and backscattered light), it is possible to excite each of the three optical phonon modes almost separately. These three polarization settings can be found when the full information about the respective crystal orientation is known (from the Raman orientation measurements). Then, the Raman intensity–polarization setting relation can be calculated for each of the phonon modes separately. By mutually calculating the ratios of the intensity of one mode to the sum intensity of the two other modes, one can easily determine the three polarization settings, where mutually one mode is dominant over the two other modes. Mapping the region of interest three times with these three special polarization settings yields then the three phonon frequency shifts $\Delta\omega_1$, $\Delta\omega_2$, and $\Delta\omega_3$ almost separately (see, for example, Ref. [12] for details). The three values for $\Delta\omega_1$, $\Delta\omega_2$, and $\Delta\omega_3$ can then be read from the maps (see, for example, Figure 14.5), and with the procedure described above, the stress tensor components (14.9) can be calculated, even though the lifting of degeneracy is not visible in the experimental spectra.

14.3.4 Additional Influences on the Phonon Frequency Shifts

14.3.4.1 Temperature

The phonon frequencies, the half widths of the Raman bands, and the intensity ratio I_{AS}/I_S of the anti-Stokes and Stokes Raman bands are temperature dependent. A rise in sample temperature leads to a decrease in phonon frequencies and an increase both in half widths and in I_{AS}/I_S ratio [43–46]. In case of silicon, the phonon frequencies are rather sensitive to changes of the sample temperature, that is, a change of $\sim$4 °C in sample temperature causes a shift of phonon frequencies of $\sim$0.1 cm^{-1} [31]. That is, slight temperature changes lead to frequency shifts that are

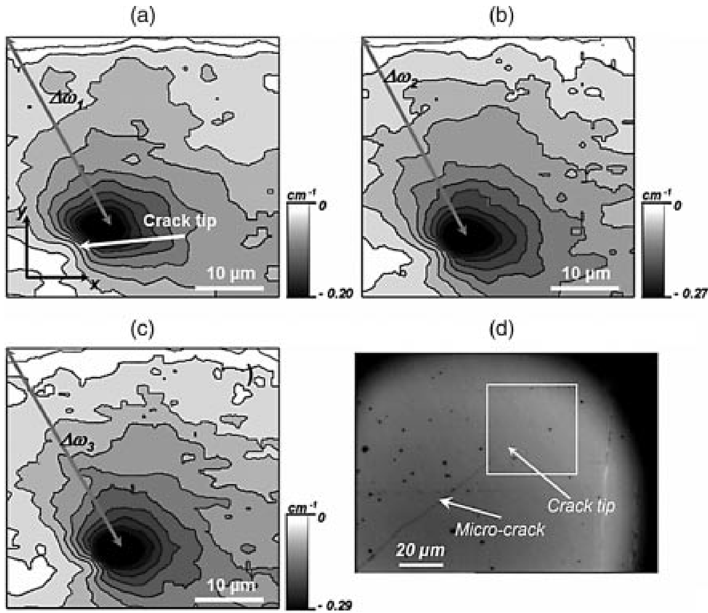

Figure 14.5 (a–c) Three maps of the phonon frequency shifts $\Delta\omega_1$, $\Delta\omega_2$, and $\Delta\omega_3$ close to the tip of a microcrack shown in (d) (white rectangle). The white rectangle in (d) (42 µm × 45 µm) marks the region where the phonon frequency maps are carried out. For the measurements, 40 × 40 measurement points were used. The three mappings correspond to the three polarization settings where each of the three phonon modes was excited separately. The calculated stress state at the tip of the microcrack is referred to the stress state at the upper left corner, which is assumed to be stress free. The ranges of the depicted gray scales are different, as they correspond to the maximum amount of frequency shifts of the respective phonon mode. By using the procedure described above, the following stress components can be determined at the indicated position (lower tip of the gray arrow) a few micrometers away from the tip:

$$\Delta\sigma = \begin{pmatrix} 57 \pm 12 & -7 \pm 3 & 0 \\ -7 \pm 3 & 54 \pm 11 & 0 \\ 0 & 0 & 19 \pm 4 \end{pmatrix} \text{MPa}$$

already above the experimental detection limit ($\approx$0,05 cm^{-1}) for the phonon frequency shifts. Thus, great care has to be taken during mechanical stress analysis with Raman spectroscopy that no significant temperature gradients arise within the sample regions of interest during the measurements. Temperature gradients during Raman measurements might arise due to a change in the laser spot size and/or a change in the laser power. Both might lead to different energy densities and therefore to different temperatures in between different measurement points. On the other hand, structural inhomogeneities within the sample (interfaces, agglomerates of defects, etc.) and on the sample surface (differences in oxide layer thickness, contaminations, etc.) can cause inhomogeneous heat generation and transport and therefore temperature gradients in between different measurement points. The average temperature within a measurement point can be roughly determined

from the I_{AS}/I_S ratio [43]. For example, in case of a HeNe laser with a power of ~6 mW on the sample and a 100*x* objective (N.A. 0.95), a stationary-state temperature within a measurement point of ~45 °C can be estimated from the I_{AS}/I_S ratio. In the experiments shown here, noticeable changes in temperature within a mapping region could be detected only in the vicinity of sample edges, where temperature differences of ~1–2 °C are measured. In the vicinity of, for example, grain boundaries or other crystal defects, changes in sample temperature that would affect the stress-induced phonon frequency shifts could not be detected.

14.3.4.2 Drift of the Spectrometer Grating

During a Raman map, the position of the optical grating might drift. This grating drift becomes noticeable in a constant drift of Raman peaks with time into one direction on the wavenumber axis. Usual drift rates lie in the range of ~0.02–0.04 cm^{-1}/h. The grating drift-induced Raman peak shifts can be easily eliminated when a plasma line of the probe laser is used as a wavenumber reference. As the plasma lines have physically fixed wavelengths [47], a drift of plasma lines with time exactly resembles the grating drift. The phonon frequency shifts that are solely produced by the sample (stress or other influences) are then obtained by subtracting the respective shift of a plasma line from the particular measured Raman peak. The experimental procedure is depicted in Figure 14.6. The Raman peaks and the plasma lines are fitted with a mixed Gaussian/Lorentzian fit function [31]. From the fitting data, the peak shifts can be determined with an accuracy of ~0.05 cm^{-1}. When the drift-compensated Raman peak shifts are then plotted versus the mapping coordinates, a corrected peak shift map is obtained from which the mechanical stress states can be detected with much higher accuracy.

14.3.5 Applications

14.3.5.1 Mechanical Stresses at the Backside of Silicon Solar Cells

Silicon solar cells are usually provided with a laminar, highly p-doped region (~10^{18}–10^{19} cm^{-3}) at the backside [47–49]. This leads to a space charge region in between the standard p-doped (10^{15}–10^{16} cm^{-3}) basis of a solar cell and the highly p-doped region at the backside (BSF). The light-generated electrons within the basis are then kept away from the back surface of the cell, which avoids charge carrier recombination at the free surface. This finally leads to a relative increase in the solar cell efficiency of ~5%–10% [50, 51]. As a dopant for this highly p-doped layer, aluminum is used. The fabrication of the BSF is usually carried out according to the following process steps [52–54]. At first, a granular mixture made of aluminum paste and glass frit (facilitates sintering) is put on the backside of the silicon wafer and heated. At 660 °C the aluminum melts and the formation of an aluminum–silicon alloy starts. At a maximum temperature of 825 °C, the entire backside of the silicon wafer is covered with a thin liquid layer of the aluminum–silicon alloy. During cooling down, a highly doped silicon-rich phase (~1% Al) starts to grow epitaxially on the wafer backside. The aluminum in this layer serves then as a dopant to generate the

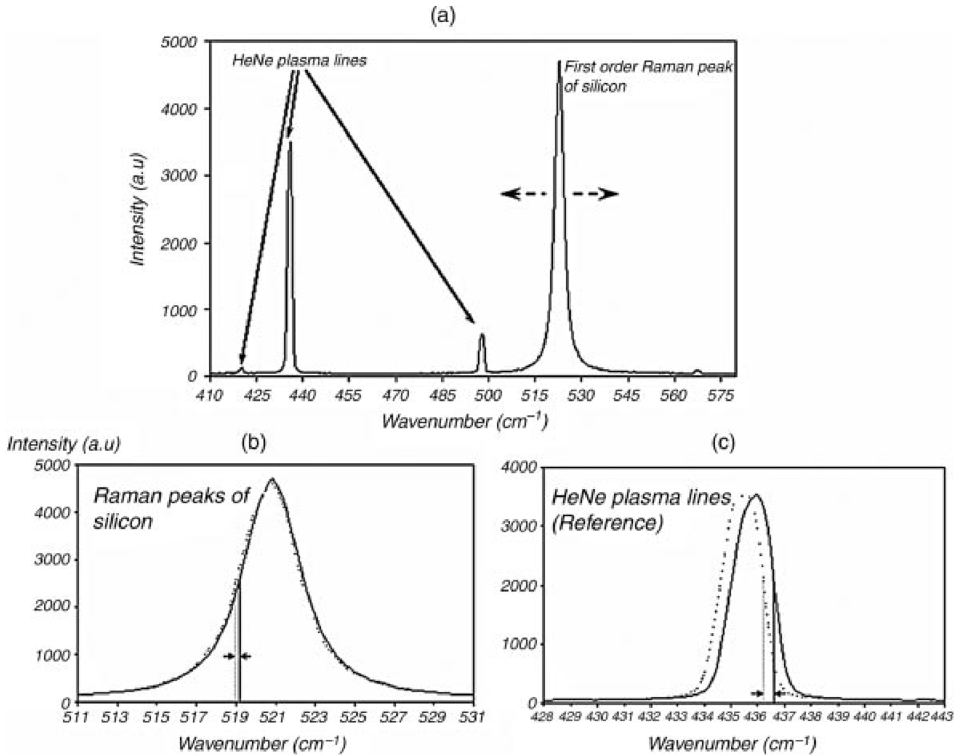

Figure 14.6 (a) Raman spectrum of silicon with the additional HeNe plasma lines. (b) Raman peak shifts of two Si Raman peaks and (c) the corresponding shifts of the plasma lines due to a spectrometer drift. The compensation of the grating drift with the plasma lines even leads to a change in sign of the Raman peak shifts in (b).

BSF. During further cooling down and after passing the eutectic point at 577 °C, the aluminum-rich phase forms a ~5–10 μm-thick layer. Underneath this layer (with reference to the front cell surface) resides a region that consists of a mixture of Al–Si alloy grains and glass frit. The optical micrographs in Figure 14.7 show cross sections of a silicon solar cell within the back surface region. The Al-doped layer (not distinguishable in the optical micrographs) resides within a region a few micrometers above the bright layer, which represents the Al-rich phase. The interface in between the Si- and the Al-rich phase exhibits an inhomogeneous shape with undulations and spikes that occur rather often. Raman maps of the phonon frequency shifts show that in the vicinity of such inhomogeneities large stress gradients on a length scale of a few micrometers occur rather frequently (maps in Figure 14.7). These large stress gradients are probably introduced during the epitaxial growth process due to the different thermal expansion coefficients of the Si-rich and the Al-rich phase. Large stresses within the back surface field region turn out to be a severe problem in view of the mechanical stability of the readily processed silicon solar cells. As the firing of the back surface field is one of the last process steps for a

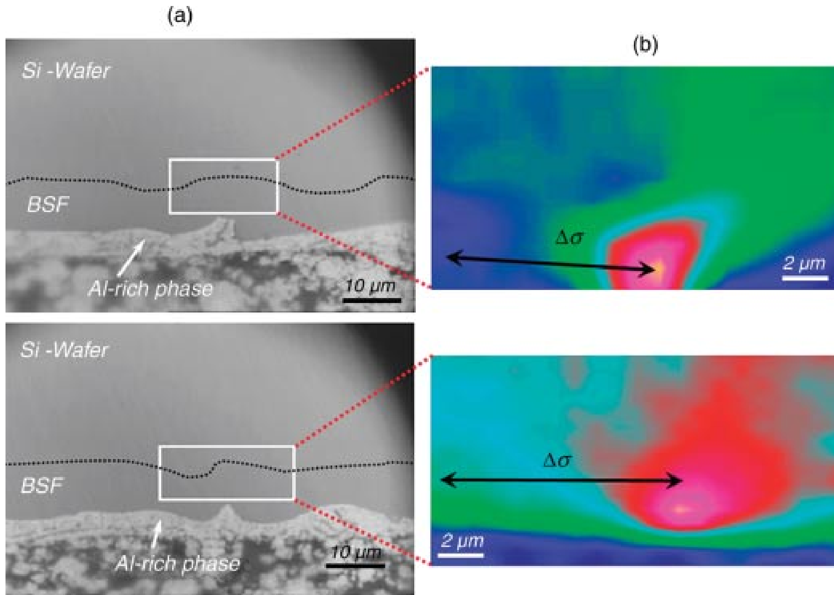

Figure 14.7 (a) Cross sections of a silicon solar cell close to the BSF region (optical micrograph). The highly Al-doped region resides up to ~10 μm above (black dotted line) the brighter Al-rich phase. (b) Maps of the frequency shifts $\Delta\omega$ of one phonon mode shortly above the spikes within the Al-rich phase (white rectangles). With reference to the positions at the left tip of the black arrows (which are assumed to be nearly stress free), the regions above the spikes are under compressive stress. The calculated stress tensors $\Delta\sigma$ at these position are given below. The corresponding stress tensor components lie in the range of ~200 MPa (compression) and ~50 MPa (compression), respectively.

$$\Delta\sigma = \begin{pmatrix} -224\pm22 & -3\pm1 & 0 \\ -3\pm1 & -197\pm19 & 0 \\ 0 & 0 & -138\pm10 \end{pmatrix} \mathrm{MPa},$$

$$\begin{pmatrix} -46\pm9 & -11\pm3 & 0 \\ -11\pm3 & -65\pm12 & 0 \\ 0 & 0 & -28\pm5 \end{pmatrix} \mathrm{MPa}$$

Si solar cell, this last step introduces sources for cracks and therefore breakage of the solar cell if additional external mechanical stress is applied due to bending/deformation of the cell. As breakage of a readily processed silicon solar cell is a much greater loss than the breakage of an unprocessed silicon wafer, inhomogeneities within the BSF region that are prone to large mechanical stress values should be avoided by better processing steps such as, for example, an optimized cooling procedure by the solar cell producers.

14.3.5.2 **Stress Fields at Microcracks in Polycrystalline Silicon Wafers**

Often cracks with lengths in the range of a few ten s of micrometers (microcracks) occur in polycrystalline silicon wafers at the edges. These microcracks are one of the main reasons for wafer breakage during the solar cell processing steps [55]. Large stress gradients on a length scale of a few micrometers occur at the tips of the microcracks. These micrometer-sized stress fields can be measured with

micro-Raman spectroscopy and from the phonon frequency shifts the mechanical stress components can be calculated. However, specific problems regarding fracture mechanics will not be discussed here, though some characteristic material parameters concerning fracture mechanics can also be determined by micro-Raman measurements [56–60]. Figure 14.5d displays the edge region of a polycrystalline silicon wafer where a microcrack of $\sim$100 μm length resides. The region close to the crack tip where the stress maps are performed is marked with a white rectangle. After determining the crystal orientation, this region is mapped with the three special polarization settings where each of the three optical phonon modes of silicon is excited separately. Figure 14.5a–c shows the maps of the three phonon frequency shifts $\Delta\omega_1$, $\Delta\omega_2$, and $\Delta\omega_3$ determined in the way described above. Again, the stress state that is measured in the vicinity of the crack tip is referred to a measurement position at the left upper corner of the mapped region. This reference position is assumed to be nearly stress free.

According to theory [61], the stresses in the vicinity of the crack tip are tensile and the amounts of the stress components lie in the range of what is expected from the three measured frequency shifts at the indicated position: $\Delta\omega_1 = -0.20\,\text{cm}^{-1}$, $\Delta\omega_2 = -0.27\,\text{cm}^{-1}$, and $\Delta\omega_3 = -0.29\,\text{cm}^{-1}$. Considering the course of the crack ($\sim$45° angle with the axis of the reference coordinate system) and the nearly symmetrical distribution of the phonon frequency shifts, it is reasonable that the two stress components in the *x*- and *y*-directions (reference coordinate system) $\Delta\sigma_{xx}$ and $\Delta\sigma_{yy}$ have nearly the same value.

14.3.5.3 **Stress States at Grain Boundaries in Polycrystalline Silicon Solar Cell Material and the Relation to the Grain Boundary Microstructure and Electrical Activity**

Micro-Raman spectroscopy, electron backscattering diffraction, and electron beam-induced current (EBIC) [62] techniques can be combined to investigate the relation between mechanical stresses at grain boundaries (GBs) in polycrystalline silicon wafers and the microstructure, as well as the electrical activity of grain boundaries. The EBSD technique is used during these investigations to determine the character of the large amount of grain boundaries present in polycrystalline silicon wafers. In principle, grain boundary characteristics can also be determined with micro-Raman spectroscopy since orientation measurements are possible (see Chapter 2). However, grain boundary analysis with EBSD works in this case faster as it is an already established and automated measurement method that is able to handle regions with a large amount of crystallites. EBIC is a standard method to investigate the electrical activity of grain boundaries. EBIC and EBSD are methods that both can be operated in a scanning electron microscope (SEM), a fact that makes it appealing to combine both methods for grain boundary and polycrystalline silicon wafer analysis. In the following experimental results, the misorientation between adjacent grains is described in terms of the Σ-value that gives the reciprocal fraction of atoms in the grain boundary plane that coincides with both adjacent lattices. Figure 14.8a shows an SEM image of a sample region within a polycrystalline silicon wafer that includes the Raman map shown in Figure 14.8b. The marker, produced by a focused ion beam (FIB), allows exact lateral correlation between the different measurement techniques.

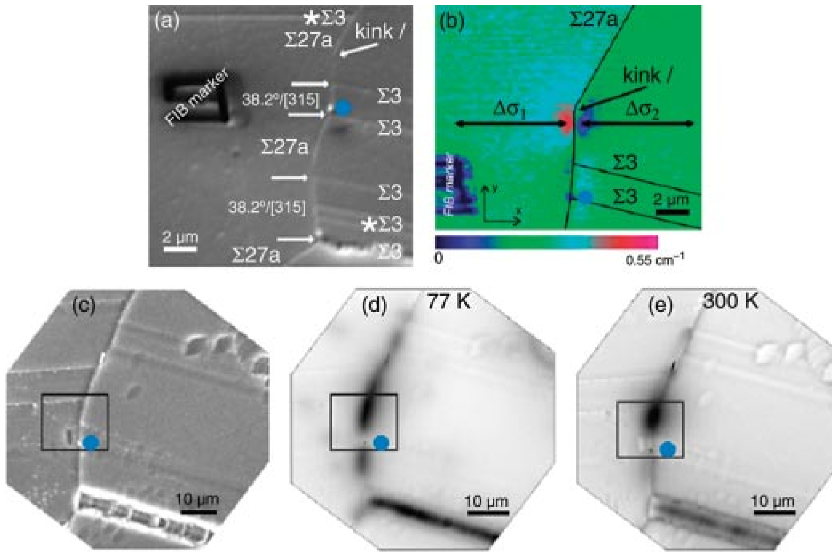

Figure 14.8 (a) SEM image of the sample region including the Raman phonon frequency map shown in (b). The compressive (red color) and tensile (blue color) stress fields around the Σ27a grain boundary is probably produced by a cluster of edge dislocations or additional inclusions located at the kink position I. (c) SEM image and the corresponding EBIC image taken at (d) 77 K and (e) 300 K, where the area enclosed by the rectangle represents the region of the Raman mapping displayed in (b). The filled blue circle visible in all images denotes the position of an inclusion.

A kink in the Σ27a grain boundary trajectory is denoted with *I* and a filled blue circle, present in all images in Figure 14.8, indicates an inclusion (probably SiC). The Raman map reveals very localized and symmetric stress fields, including both compressive (red region in the map) and tensile (blue) stresses, in the vicinity of the Σ27a grain boundary, close to the kink *I*. The reason for a stress field with such kind of shape might be the presence of dislocations within the grain boundary or additional inclusions. A detailed polarization-dependent Raman analysis of the stress fields on either side of the indicated grain boundary gives the following two stress tensors (referring to the indicated reference coordinate system) that again have been evaluated relative to the indicated positions away from the grain boundary and which are assumed to be almost stress free.

$$\Delta\sigma_1 = \begin{pmatrix} -40 \pm 10 & -14 \pm 1 & 0 \\ -14 \pm 1 & -38 \pm 10 & 0 \\ 0 & 0 & -25 \pm 10 \end{pmatrix} \text{MPa}$$

$$\Delta\sigma_2 = \begin{pmatrix} 33 \pm 10 & -7 \pm 1 & 0 \\ -7 \pm 1 & 31 \pm 10 & 0 \\ 0 & 0 & 34 \pm 10 \end{pmatrix} \text{MPa} \qquad (14.8)$$

Though the stress fields become visible in the Raman map (Figure 14.8b), the determined stress components are rather small and close to the resolution limit of ~20 MPa. The EBIC images (Figure 14.8d and e) show a strong contrast (i.e., a reduced carrier lifetime) close to the kink *I* both at 77 K and at 300 K and a contrast variation with temperature along the Σ27a grain boundary. The region enclosed by the rectangle corresponds to the stress map shown in Figure 14.8b. By comparing these images, it becomes clear that the stressed area close to the kink *I* and the stress-free area above it exhibit strong but similar EBIC contrasts and therefore similar electrical activity. This example shows that mechanical stresses of this magnitude are probably not able to change the recombination activity of polycrystalline silicon due to a stress-induced change in band structure. However, as the largest EBIC contrast is visible at the position of the kink *I*, where the dipole-like stress field resides, most probably a cluster of edge dislocations or inclusions are responsible for the visible stress field.

14.3.6
Comparison with other Stress/Strain Measurement Methods

Besides micro-Raman spectroscopy, there are a few other methods that are frequently used to determine mechanical stress/strain in solids. But again, each of these methods also has its specific drawbacks concerning practical applicability, lateral resolution, or the destructive nature of the measurement technique. In the case of stress/strain analysis in crystals by standard X-ray diffraction, all the stress/strain tensor components can be detected with some effort [63]. But the method is rather time consuming, the lateral resolution of the stress analysis is small, and the obtained data are stress values that are averaged over a rather large sample volume. Much better lateral resolution can be obtained with the brilliant X-ray radiation of a synchrotron, but the measurements then become even more complex. With stress-induced birefringence, that is, the analysis of stress-induced optical anisotropies in crystals [64], the mechanical stress/strain distributions within a large sample region (a few cm^2) can be detected rather fast. However, the lateral resolution of stress-induced birefringence is much too low to analyze stresses on the (sub) micrometer scale and in addition, only the differences of absolute values (i.e., without sign) of the principal stress components can be determined. Mechanical stress analysis on the nanometer scale can be performed with the convergent beam electron diffraction (CBED) technique in a transmission electron microscope [65]. But as CBED needs the preparation of thin samples for the TEM, this technique is destructive and needs rather complex instrumentation. In addition, as the investigated TEM samples are rather thin, artifacts such as thin foil relaxation [66] lead to a change in stress states with respect to the stresses that were present in the unprepared samples.

14.4
Measurement of Free Carrier Concentrations

Highly doped regions in silicon solar cells are important for the proper and effective operation of solar cells. While an n-doped emitter region is produced by dopant

(phosphor) diffusion from the gas phase, the highly p-doped back surface field is generated by alloying silicon with aluminum from an Al paste at the back surface of a silicon solar cell [49–51] (as already described in Chapter 3). Usually, the exact free carrier concentrations and gradients within the BSFs are measured by the electrochemical capacitance–voltage (ECV) method [67, 68]. This method measures the free carrier concentrations rather accurately, but it lacks good lateral resolution as the measurement results are integrated and therefore averaged, over an area of a few mm^2 at the back surface of the respective solar cell. Raman-specific Fano [69–71] resonances, combined with small-angle beveling techniques, can be used to determine the concentration of free charge carriers within the BSF regions and to map the free hole concentration and gradients on an effective length scale of a few tens of nanometers. The basic features of Raman-specific Fano resonances will be shortly discussed and measurement results are presented, which show that the free carrier concentrations within the BSF regions can be qualitatively and quantitatively mapped and analyzed by micro-Raman spectroscopy.

14.4.1
Theoretical Description

As discussed in the original articles of Fano [69–71], a resonant interaction of a discrete energy level with a continuum of energy levels in a given system leads to a characteristic Fano-type peak asymmetry that can be usually observed during spectroscopic experiments of such kind of quantum mechanically coupled systems (see Figure 14.9).

Cerdeira and other authors [72–76], explain the occurrence of the Fano-type peak asymmetry of the F_{2g} Raman band of highly p-doped silicon with a resonant

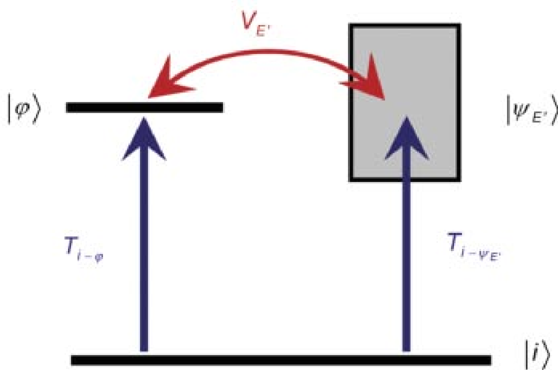

Figure 14.9 Interaction of a discrete state $|\varphi\rangle$ with a continuum of states $|\psi_{E'}\rangle$ that leads to Fano resonances. From an initial state $|i\rangle$ the system can be excited into the continuum of states and into the discrete state by the independent transition operators $T_{i-\varphi}$ and $T_{i-\psi_{E'}}$, respectively. If there is an interaction $V_{E'}$ between the discrete state and the continuum, the transition probabilities interfere, leading to Fano-type peak asymmetries that are observable in spectroscopic experiments.

interaction of the discrete optical phonon (phonon Raman scattering) state with the continuum of energy levels, corresponding to the hole transitions from filled to empty valence band states (electronic Raman scattering [77, 78]) due to electron–phonon coupling. According to Fano's fundamental theory, if a system exhibits an energetic continuum of states $|\psi_{E'}\rangle$ and a discrete state $|\varphi\rangle$, the corresponding elements of the Hamiltonian matrix can be written as

$$\begin{aligned} \langle\varphi|H|\varphi\rangle &= E_{\varphi} = \hbar\Omega \\ \langle\psi_{E'}|H|\varphi\rangle &= V_{E'} \\ \langle\psi_{E''}|H|\psi_{E'}\rangle &= E\delta(E''-E') \end{aligned} \tag{14.12}$$

The parameter $V_{E'}$ represents the coupling strength of the discrete state with the continuum of states, H is the Hamilton operator, and Ω specifies the frequency that corresponds to the respective discrete state. The new eigenvector $|\Psi_E\rangle$ of the coupled system, which now corresponds to the new composite state given by Eq. (14.12) then becomes a linear combination of the discrete eigenstate and the continuum of states, that is, $|\Psi_E\rangle = a_E|\varphi\rangle + \int b_{E'}|\psi_{E'}\rangle \mathrm{d}E'$, where the coefficients a_E and b_E are functions of the energy. If there is an arbitrary initial state $|i\rangle$ and a respective dipole transition operator T (see Figure 14.9), the transition probability to the unperturbed continuum $|\psi_{E'}\rangle$ becomes $\left|\langle\psi_{E'}|T|i\rangle\right|^2$ and the transition probability to the new composite state $|\Psi_E\rangle$ is defined as $\left|\langle\Psi_E|T|i\rangle\right|^2$. The ratio of the transition probabilities to the new composite state and to the unperturbed continuum gives then the general shape of the measured spectral peaks that are now distorted by the occurring Fano resonances [69–71]

$$\frac{|\langle\Psi_E|T|i\rangle|^2}{|\langle\psi_{E'}|T|i\rangle|^2} = \frac{(q+\varepsilon)^2}{1+\varepsilon^2} \tag{14.13}$$

where ε indicates the renormalized energy or, in the spectroscopic experiments, the renormalized wavenumber parameter $\varepsilon = 2(\Omega-\Omega_{\mathrm{Max}})/\Gamma$. Ω_{Max} describes the position of the peak maximum, which is also slightly shifted by the Fano interaction, and Γ describes the linewidth of the peak, where $\Gamma = \Gamma_0 + \Delta\Gamma$ with Γ_0 the linewidth in the absence of a continuum of states, and $\Delta\Gamma$ describes the symmetric contribution of the Fano interaction to the total linewidth of the peak. The parameter q in Eq. (14.13) is frequently called the symmetry parameter and can be expressed as

$$q = \frac{\langle\Phi|T|i\rangle}{\pi\langle\varphi|H|\psi_E\rangle\langle\psi_E|T|i\rangle} = \frac{\langle\Phi|T|i\rangle}{\pi\, V_{E'}^{*}\langle\psi_E|T|i\rangle} \tag{14.14}$$

The state $|\Phi\rangle$ defines the discrete state $|\varphi\rangle$ modified by the additional continuum of states, that is, $|\Phi\rangle = |\varphi\rangle + P\int V_{E'}|\psi_{E'}\rangle/(E-E')\,\mathrm{d}E'$. P designates the principal part of the integral. The symmetry parameter q determines the characteristic asymmetric shape of a spectral peak influenced by Fano resonances. The spectral line becomes symmetric if $q \to \infty$, whereas if $q \to 0$, the more asymmetric the peak becomes. Especially for highly doped silicon, $1/q$ becomes roughly proportional to the free carrier concentration [73, 74, 79]. The value of $1/q$ is positive in case of highly p-doped

silicon and negative in case of highly n-doped silicon, whereas the sensitivity of experimentally measurable Fano resonances is much higher in case of p-doped than in case of n-doped silicon [79–83].

14.4.2
Experimental Details

14.4.2.1 Small-Angle Beveling and Nomarski Differential Interference Contrast Micrographs

For the following examples of Raman-based dopant analysis, readily processed, standard polycrystalline silicon solar cells, provided with a back surface field, were cut into pieces (area of a few cm^2). These pieces were put on wedges with opening angles α ranging from $\sim$5 to 10°. The samples residing on the wedges were then embedded in a cylindrical shaped basin with resin. After drying, the embedded samples were mechanically and chemically polished. Finally, all samples were Secco [17] etched to make the crystal defects (random-, twin boundaries, dislocations, etc.) and the back surface field region visible. By the small-angle beveling process, the length scales of the free carrier concentration profiles in the solar cell samples are artificially increased in one direction by a stretching factor $s(\alpha)$, which solely depends on the opening angle α. For the stretching factor $s(\alpha)$, the simple relation holds (see Figure 14.10):$d^* = d/\sin(\alpha) = ds(\alpha)$, where d^* is the increased but oblique thickness of the solar cell after the small-angle beveling process and d indicates the original thickness.

The small-angle beveling process reveals much more details of the BSF shape and its adjacent microstructure than a standard polishing process of the cross section of a silicon solar cell would reveal. On the other hand, small-angle beveling introduces some irritating artifacts, such as island formation within an originally wrinkled but continuous interface (see Figure 14.10). The highly p-doped BSF region exhibits a different Secco etching rate compared to the rest of the crystal due to the additional Al atoms in the Si crystal lattice. Therefore, a sharp step of a few hundreds of nanometers in height (depending on the etching time) arises in between the highly p-doped BSF region and the usually weakly ($\sim 10^{15}\,cm^{-3}$–$2\times10^{16}\,cm^{-3}$) boron-doped bulk wafer region after etching. This step, as well as the trenches and pitches produced by the grain boundaries and dislocations, becomes visible in a Nomarski differential interference contrast (NDIC) microscope [84, 85]. Figure 14.11a–c shows some NDIC images of the BSF–bulk wafer interface region, where the different

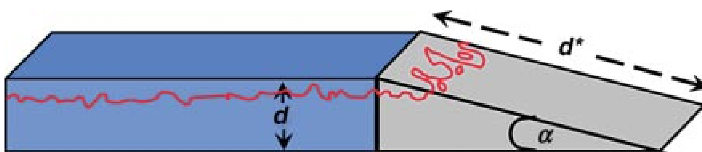

Figure 14.10 Schematic drawing of a piece of a standard silicon solar cell containing a back surface field (above red line) after small-angle beveling. Due to the small-angle beveling process, the original thickness d of the cell is increased to an apparent thickness d^*.

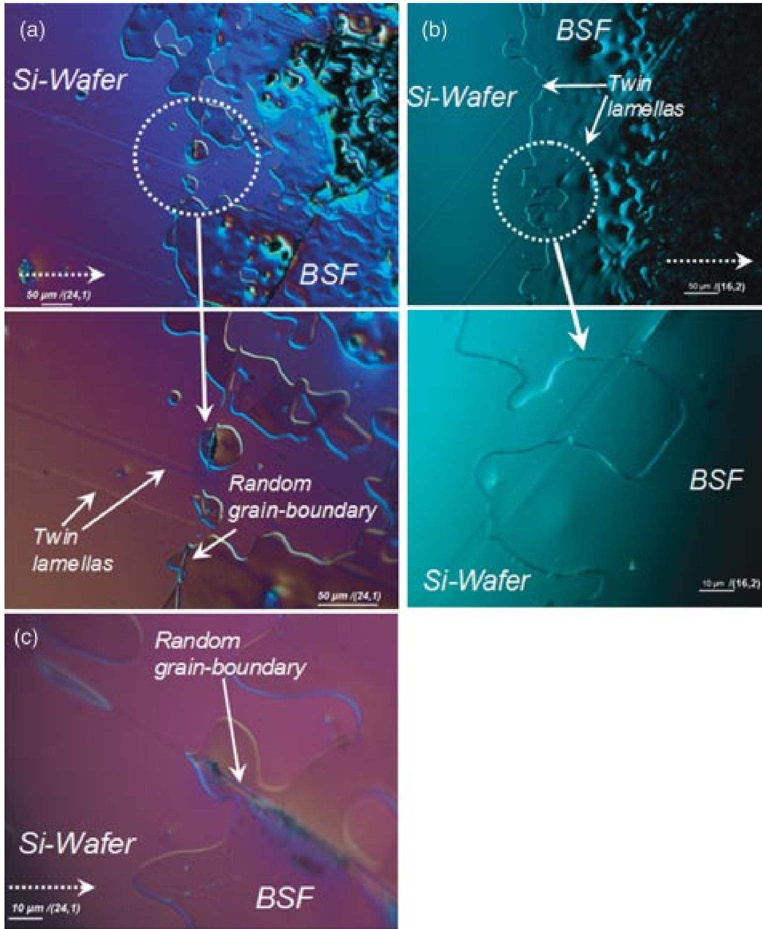

Figure 14.11 Images of the BSF–bulk wafer interface region of standard polycrystalline silicon solar cells. The images were taken with a Nomarski differential interference contrast microscope that allows the visualization of the height difference that occurs after Secco etching in between the BSF and the weakly p-doped bulk wafer region. The stretching factors $s(\alpha)$ are given in brackets above the scale bars and the stretched directions are indicated by the white dotted arrows.

samples were beveled by using different wedge angles. The resulting stretching factors $s(\alpha)$ are given in brackets above the scale bars and the stretched directions are indicated by the dotted white arrow.

14.4.2.2 **Evaluation of the Raman Data**

For the Raman measurements, regions of interest within the small-angle beveled samples were chosen and mapping areas were defined. Within the mapping regions, Raman spectra of the threefold degenerate first-order optical phonon (F_{2g}) mode of

silicon were acquired every 1–3 μm in both x- and y-directions. All Raman measurements shown here were performed with the 633 nm emission of a HeNe laser, as the peak asymmetry due to Fano resonances becomes more pronounced when longer excitation wavelengths are used [73]. To obtain quantitative information about the free carrier concentrations from Raman mappings, the intensity $I(\Omega, q)$ of the first-order Si Raman peak should be fitted with a function resulting from Eq. (14.13):

$$I(\Omega, q) = I_0 \frac{[q + 2(\Omega - \Omega_{\mathrm{Max}})/\Gamma]^2}{1 + [2(\Omega - \Omega_{\mathrm{Max}})/\Gamma]^2} \tag{14.15}$$

Practically, Ω simply represents the wavenumber axis (in cm^{-1}) and I_0 is just a scaling factor. If the exact values of the physically important parameters q, Ω_{Max}, and Γ are needed, all Raman spectra of interest should be fitted with Eq. (14.15). However, as Raman mappings usually consist of many thousand measurement points, fitting all the corresponding spectra with iterative routines would take unnecessarily long time. To determine the free carrier concentrations in highly doped regions with sufficient accuracy, mainly the values of the symmetry parameter q are of importance. The symmetry parameter q can be easily and with sufficient accuracy determined from the experimental data by an evaluation of the integrated intensity of the Raman peak portion I_{R} that becomes asymmetric due to the occurring Fano interferences. That is, one has to evaluate the intensity ratio $R(q) = I_{\mathrm{R}}/I_{\mathrm{tot}} = I_{\mathrm{R}}/(I_{\mathrm{L}} + I_{\mathrm{R}})$, where I_{L} describes the left peak portion (see Figure 14.12). $R(q)$ is a function that mainly depends on the symmetry parameter q. The details can be found in Ref. [86]. The maps shown in this chapter plot the $R(q)$ values given above, where in general

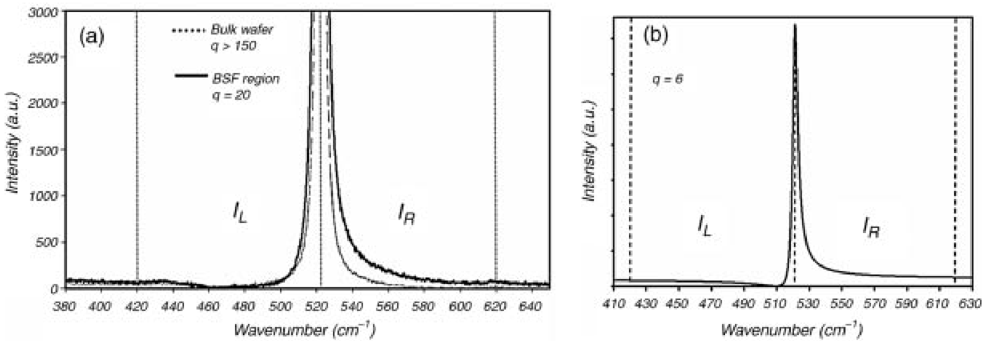

Figure 14.12 (a) Baselines of the two first-order Raman peaks of silicon measured within the bulk wafer (dashed gray curve) and the BSF region (continuous black curve). The spectra were acquired from a different map region (not shown here) within the same sample. The two peaks are normalized and therefore the maximum intensities are the same (not visible in the plot). High p-doping leads to a broadening of the higher wavenumber flank of the Raman peak (q positive but smaller) and to a larger Γ value, which manifests in also slightly broader lower wavenumber flank of the Raman peak. (b) Calculated Fano Raman peak for a hypothetical q-value of $q = 6$ (extremely high p-doping). With the two integrated peak intensities I_{L} and I_{R}, the function $R(q) = I_{\mathrm{R}}/I_{\mathrm{tot}} = I_{\mathrm{R}}/(I_{\mathrm{L}} + I_{\mathrm{R}})$ is defined from which the symmetry parameter q can be determined rather fast but with less accuracy.

the yellow/red color coding represents high $R(q)$ values and therefore small q-values (high p-doping levels), and the blue/black color coding displays the opposite conditions.

14.4.2.3 Calibration Measurements

It is possible to determine the free carrier concentration levels in silicon from the q-parameter directly from theoretical calculations. However, it has been shown in literature [82] that the theoretically calculated free carrier concentrations substantially deviate from the experimentally determined ones (by one order of magnitude). Therefore, it is preferable to use data obtained from ECV to calibrate the Raman data. The q-parameters and the free carrier concentration levels that are obtained from an analysis of the Raman peaks are calibrated in the following way: The free hole concentration profiles within the BSF region of a standard silicon solar cell were first measured with the ECV method. Then a piece of the same solar cell was small-angle beveled and Secco etched in the manner as described above. The BSF region was then analyzed by Raman spectroscopy. Depending on the solar cell, the standard free hole concentration level within the bulk wafer region lies usually in the range of $\sim 5 \times 10^{15}$ cm^{-3}–2×10^{16} cm^{-3}. According to the literature [73, 79], the standard p-doping levels of the respective bulk wafers still produce some slight Fano resonances when the 633 nm excitation wavelength is used, but the Raman peaks become almost symmetric in practice and the values for the parameter q take values larger than ~ 150. The reciprocal symmetry parameter $1/q$ is roughly proportional to the free hole concentration in silicon [73–75]. Therefore, the free hole concentrations that are obtained from the ECV measurements can be plotted versus $1/q$ (obtained from the Raman measurements) resulting in a roughly linear correlation between the free hole concentration and the $1/q$ values. This plot is shown in Figure 14.13. The obtained linear calibration curve is used for the following free hole concentration measurements and maps.

14.4.3 Experimental Results

The left image in Figure 14.14 shows an enlarged optical micrograph of the spike-containing BSF feature already shown in Figure 14.11c. The right image represents the Raman map of the Fano asymmetry (ratio $R(q)$) produced by the high p-doping within the BSF region. At the six positions, marked with an asterisk, the symmetry parameter q and the free hole concentration were determined by the more accurate peak fitting routine using Eq. (14.15) (see Table 14.1) rather than by the less accurate inversion of the experimentally determined function $R(q)$. The highest free hole concentration levels are measured at positions (position 4, 5, 6) in the vicinity of a random grain boundary (dotted line). These regions occur much darker in the optical micrograph (red arrow), compared to the bright bulk wafer region and the slightly darker BSF region. It is assumed that the somewhat higher etching rate at the random grain boundaries is responsible for the dark contrast: close to the random grain boundaries, the silicon becomes rather thin due to the higher etching rate. The dark Al-rich phase underneath the Si-rich phase (BSF region) becomes then better visible

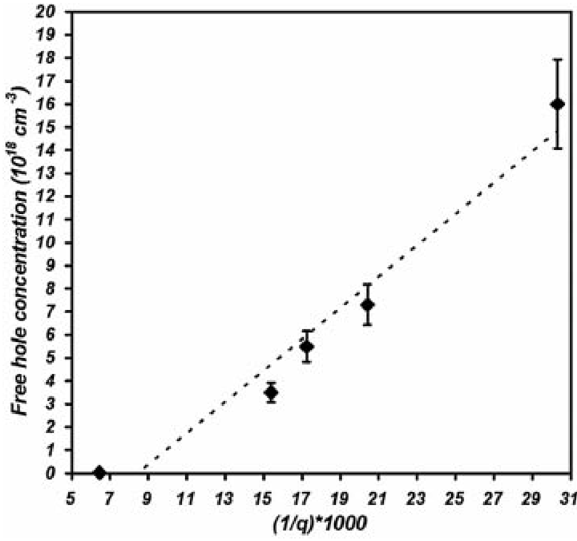

Figure 14.13 Free hole concentrations within the BSF region determined by the ECV method plotted versus the reciprocal Fano symmetry parameter $1/q$. The roughly linear correlation is indicated by the dotted calibration line. This line is used to determine the free hole concentrations within the BSF regions from the following Raman maps. The error bars account for the inaccuracy of the ECV measurements, which results from spatial variations of the p-dopant concentrations within a single solar cell.

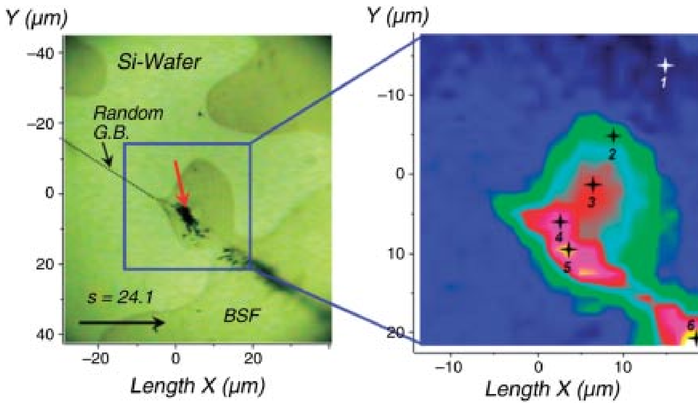

Figure 14.14 (a) Optical micrograph of the spike-containing BSF feature already shown in Figure 14.11c. (b) Raman map of the Fano-induced peak asymmetry produced by the high p-doping within the BSF region. At six positions, marked with an asterisk, the symmetry parameter q and the free hole concentrations were determined by the more accurate peak fitting routine using Eq. (14.15) (see Table 14.1).

Table 14.1 Symmetry parameters q and the resulting reciprocal values $1/q$ as well as the free hole concentrations determined by Raman measurements.

Position	q	$1/q$ * 1000	Carr. Conc. (10^{18} cm^{-3})
1	>150	<6.67	<0.025
2	65	15.38	4.7
3	54	18.52	6.8
4	51	19.61	7.6
5	39	25.64	11.7
6	29	34.48	17.7

The data correspond to the six positions, marked with an asterisk in the Raman map shown in Figure 14.14.

and influences the free carrier concentration measurements due to the additional Al atoms. The q-value and the corresponding free hole concentration level at position 3 probably gives a more accurate value of the free hole concentration contained in the major part of the BSF region. The fact that the small spike within the BSF–bulk wafer interface close to the random grain boundary can be resolved by the Raman map shows how good the lateral resolution of the combined small-angle beveling Raman measurements within these regions are. In Figure 14.12, the baselines of the two first-order Raman peaks of silicon, measured within the bulk wafer (dotted gray) and the BSF region (continuous black), are displayed. High p-doping (black curve) leads not only to a broadening of the higher wavenumber flank of the Raman peak (q positive but small) but also to a larger Γ (peak width) value, which manifests in an also slightly broader lower wavenumber flank of the silicon Raman band. The continuous black curve in Figure 14.12a shows one of the maximal Fano-induced peak asymmetries of all the Raman measurements presented here. The corresponding free hole concentration level is $>2 \times 10^{19}$ cm^{-3}.

The transition from the standard low doping level within the bulk wafer (dark blue regions) to the highly p-doped regions (BSF) usually takes place within less than $\sim$3 μm in the Raman maps. If we take into account that this transition elongation into the small-angle beveled direction has to be divided by the stretching factor $s(\alpha)$, the effective transition length would lie in the range of $\sim$250–700 nm. However, it can be assumed that the dopant atom concentrations at the bulk wafer–BSF interface follows the theoretical step functional shape and that the measured gradient of the free hole concentration results from (1) the blurring effect of the focused (and sometimes defocused) laser spot and (2) the elongation of the free hole diffusion of a few hundreds of nanometers [87] into the weakly doped bulk wafer region. The BSF region shown in the optical micrographs and Raman maps in Figure 14.14 exhibits a rather exceptional rough and wrinkled shape. One reason for the unusual shape is that in this case a large stretching factor $s(\alpha)$ was used, resulting in small-angle beveling artifacts such as island formation and rather distorted BSF shapes. Another reason is that the region shown in Figure 14.14 contains a more complex microstructure, for example, random boundaries, leading to a pronounced spike formation at the BSF–bulk wafer interface. The Raman map shown in Figure 14.15 represents

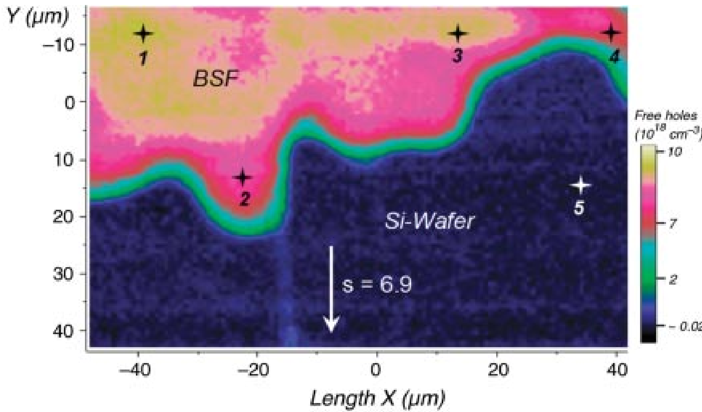

Figure 14.15 Raman map that represents a more typical BSF region (~95% of all BSF regions) within the investigated samples. In this case, a rather small stretching factor ($s(\alpha) = 6.9$) was used, avoiding the artificial island formation. No random or twin boundaries were present in the analyzed sample region, leading to a much more homogeneous and smooth BSF shape.

the shape of a more typical BSF region within the investigated samples. In this case, a rather small stretching factor ($s(\alpha) = 6.9$) was used, avoiding the artificial island formation. Also, no random or twin boundaries are present in the analyzed sample region, leading to a more homogeneous and smooth BSF shape. As in the sample region presented in Figure 14.14, the elongation of the BSF to bulk wafer free hole concentration gradient is ~3 μm, resulting again from the blurring effect due to the finite size of the laser spot and the free hole diffusion into the weakly doped bulk wafer region. The variations in the q parameter in this case are rather small (43–51), corresponding to small free hole concentration variations of $7.6 \times 10^{18}\,cm^{-3}$–$10.1 \times 10^{18}\,cm^{-3}$. Again, there are five measurement points (marked with an asterisk) that were analyzed in more detail. The obtained data are presented in Table 14.2.

Table 14.2 Symmetry parameters q and the resulting reciprocal values $1/q$ as well as the free hole concentrations determined by Raman measurements.

Position	q	$1/q$ * 1000	Carr. Conc. (10^{18} cm^{-3})
1	43	23.26	10.1
2	49	20.41	8.1
3	46	21.74	9.0
4	51	19.61	7.6
5	>150	<6.67	<0.025

The data correspond to the five positions, marked with asterisks in the Raman map shown in Figure 14.15.

14.4.4 Comparison with other Dopant Measurement Methods

Besides Raman spectroscopy and the ECV method, there are two other dopant concentration measurement techniques that are worth mentioning as they are frequently used. The standard method when boron-doped silicon samples are analyzed is secondary ion mass spectroscopy (SIMS) [88–90]. This technique measures directly the concentrations of dopant atoms and not the free carrier concentrations. With SIMS it is possible to perform mapping of dopant atom concentrations with ~ μm resolution in two or even three dimensions and to distinguish between the different dopant species. However, SIMS needs high-vacuum equipment that makes the method complex and expensive. Another drawback of SIMS is that quantitative measurement results are often difficult to obtain, especially if silicon samples that are highly doped with other dopants than boron (e.g., aluminum) are investigated [91]. A method that measures lateral free carrier concentration gradients instead of absolute values of dopant concentrations is the lateral photoscanning method (LPS) [92]. But the lateral resolution of the LPS method is limited to ~30 μm and therefore not suited to analyze and map free carrier concentration variations within the few micrometers thick BSF and other highly doped regions (e.g., the emitter) within a silicon solar cell.

14.5 Concluding Remarks

Micro-Raman spectroscopy has been established as a valuable analysis tool in semiconductor science and technology as well as microelectronics in the past decade. Micro-Raman spectroscopy has already become a standard instrument in research and development departments of most semiconductor and microelectronics industries. There, Raman spectroscopy is used to analyze mechanical stress, composition, dopant distributions, and crystallinity within semiconductor devices or for failure analysis on the submicrometer scale.

However, in photovoltaic science and technology, Raman spectroscopy has emerged only in the past few years from a niche method to a routinely used analysis tool. One reason for the delayed establishment of Raman spectroscopy in this field might be that the usually more complex microstructure of photovoltaic materials made it difficult to simply transfer the measurement and evaluation procedures used in microelectronics to photovoltaic devices. Another reason is that until the last few years there was no real need for solar cell material analysis with Raman spectroscopy. Due to the rather thick and therefore mechanically stable silicon wafers, questions concerning the mechanical stress/strain states and wafer breakage played only a minor role. Due to the already well-established and automated dopant analysis methods (e.g., ECV measurements), there was also no need to develop a new doping analysis tool based on Raman spectroscopy. However, things changed drastically, as the solar cell producers were recently forced to reduce the thickness of the bulk silicon

wafers or to use thin film solar cell concepts in order to reduce the overall solar cell production costs and to finally offer photovoltaic energy at competitive market prices. However, as thinner wafers and thin silicon films (a few micrometer thick) are prone, to a greater extent, to breakage due to internal mechanical stress, crack formation, and propagation, mechanical stress/strain analysis on the submicrometer scale has become increasingly important. As micro-Raman spectroscopy is one of the few methods that enables quantitative and nondestructive mechanical analysis with submicrometer spatial resolution and offers quantitative analysis of dopant concentrations along the way, this method has become particularly important in solar material characterization in the past few years. Though Raman measurements can be performed rather fast and easily in practice, the interpretation of the measurement results can become increasingly tricky and puzzling. Therefore, the main purpose of this chapter was to equip the potential applicant of Raman spectroscopy in the field of photovoltaics with the necessary physical background and knowledge of spectroscopy of solids to use the presented methods effectively or to improve and further develop the described evaluation procedures.

In addition to mono- and polycrystalline silicon wafers, there are many other solar cell material systems where Raman spectroscopy might also serve as an important analysis tool in future, but not discussed in this chapter. For example, in amorphous or microcrystalline laser-crystallized thin film solar cells, the crystalline Si/amorphous Si ratio and information about the grain sizes could be determined and mapped with micro-Raman spectroscopy. Also in chalcopyrite-based solar cells, Raman spectroscopy could serve to analyze the composition, the material structure, or the influences of mechanical stresses.

A rather new and promising field in photovoltaics are organic solar cells where concepts such as dye- or polymer-based devices are already or close to marketability. However, especially in the field of organic photovoltaics, there are still some phenomena and effects that are not fully understood, for example, the exact path of charge carrier transport or how to enhance the carrier transport by additional constituents and better ordering [93]. In this branch of photovoltaics, Raman spectroscopy of organic materials, that is, the analysis of chemical bonds and their frequency shifts due to different surroundings, might serve as an important technique in the future to elucidate these open but important questions.

References

1 De Wolf, I., Maes, H.E., and Jones, S.K. (1996) *J. Appl. Phys.*, **79**, 7148.
2 De Wolf, I. (1996) *Semicond. Sci. Technol.*, **11**, 139.
3 De Wolf, I. (1999) *J. Raman Spectrosc.*, **30**, 877.
4 Michler, J., Kaenel, Y.V., Stiegler, J., and Blank, E. (1998) *J. Appl. Phys.*, **83**, 187.
5 Dietrich, B. and Dombrowski, K.F. (1999) *J. Raman Spectrosc.*, **30**, 893.
6 Loudon, R. (1964) *Adv. Phys.*, **13**, 423.
7 Mizoguchi, K. and Nakashima, S. (1989) *J. Appl. Phys.*, **65**, 2583.
8 Yu, P.Y. and Cardona, M. (eds) (1996) *Fundamentals of Semiconductors*, Springer, Berlin.

9 Hopkins, J.B. and Farrow, L.A. (1986) *J. Appl. Phys.*, **59**, 1103.

10 Secco D' Aragona, F. (1972) *J. Electrochem. Soc.*, **119**, 948.

11 Damen, T.C., Porto, S.P.S., and Tell, B. (1966) *Phys. Rev.*, **142**, 570.

12 Becker, M., Scheel, H., Christiansen, S., and Strunk, H.P. (2007) *J. Appl. Phys.*, **101**, 063531.

13 Kendall, D.L. (1979) *Ann. Rev. Mater. Sci.*, **9**, 373.

14 Geis, M.W., Smith, H.I., Tsaur, B.Y., Fan, J.C.C., Maby, E.W., and Antoniadis, D.A. (1982) *Appl. Phys. Lett.*, **40**, 158.

15 Bezjian, K.A., Smith, H.I., Carter, J.M., and Geis, M.W. (1982) *J. Electrochem. Soc.*, **129**, 1848.

16 Williams, D.B. and Carter, C.B. (2009) *Transmission Electron Microscopy: A Textbook for Materials Science*, Springer, Berlin.

17 Joy, D.C., Newbury, D.E., and Davidson, D.L. (1982) *J. Appl. Phys.*, **53**, R81.

18 Nishioka, T., Shinoda, Y., and Ohmachi, Y. (1983) *Appl. Phys. Lett.*, **43**, 92.

19 Sandercock, J.R. (1972) *Phys. Rev. Lett.*, **28**, 237.

20 Anastassakis, E., Pinczuck, A., Burstein, E., Pollack, F.H., and Cardona, M. (1970) *Solid State Commun.*, **8**, 133.

21 Menendez, J. (2000) Characterization of bulk semiconductors using Raman spectroscopy, in *Raman Scattering in Materials Science* (eds W.H. Weber and R. Merlin), Springer, Berlin, pp. 55–103.

22 Ganesan, S., Maradudin, A.A., and Oitmaa, J. (1970) *Ann. Phys.*, **56**, 556.

23 Callen, H. (1968) *Am. J. Phys.*, **36**, 735.

24 Anastassakis, E. and Burstein, E. (1971) *J. Phys. Chem. Solids*, **32**, 563.

25 Cerdeira, F. and Cardona, M. (1972) *Phys. Rev. B*, **5**, 1440.

26 Melendez-Lira, M., Menendez, J., Windl, W., Sankey, O.F., Spencer, G.S., Sego, S., Culbertson, R.B., Bair, A.E., and Alford, T.L. (1997) *Phys. Rev. B*, **54**, 12866.

27 Kittel, C. (1996) *Introduction to Solid State Physics*, John Wiley & Sons, Inc., New York.

28 Anastassakis, E. and Burstein, E. (1971) *J. Phys. Chem. Solids*, **32**, 313.

29 Chandrasekhar, M., Renucci, J.B., and Cardona, M. (1978) *Phys. Rev. B*, **17**, 1623.

30 Anastassakis, E., Cantarero, A., and Cardona, M. (1990) *Phys. Rev. B*, **41**, 7529.

31 De Wolf, I., Jimenez, J., Landesman, J., Frigeri, C., Braun, P., Da Silva, E., and Calvet, E. (1998) Raman and Luminescence spectroscopy for microelectronics, *Catalogue of Optical and Physical Parameters, Nostradamus* Project SMT4-CT-95-2024, Published by the European commission.

32 Bonera, E., Fanciulli, M., and Batchelder, D.N. (2002) *Appl. Phys. Lett.*, **81**, 3377.

33 Bonera, E., Fanciulli, M., and Batchelder, D.N. (2003) *J. Appl. Phys.*, **94**, 2729.

34 Puech, P., Pinel, S., Jasinevicius, R.G., and Pizani, P.S. (2000) *J. Appl. Phys.*, **88**, 4582.

35 Narayanan, S., Kalidindi, S.R., and Schadler, L.S. (1997) *J. Appl. Phys.*, **82**, 2595.

36 Loechelt, G.H., Cave, N.G., and Menendez, J. (1999) *J. Appl. Phys.*, **86**, 616.

37 Brotherton, S.D., Ayres, J.R., Edwards, M.J., Fisher, C.A., Glaister, C., Gowers, J.P., McCulloch, D.J., and Trainor, M. (1999) *Thin Solid Films*, **337**, 188.

38 Hellwege, K.H. (1988) *Einführung in die Festkörperphysik*, Springer, Berlin (in German).

39 Ito, T., Azuma, H., and Noda, S. (1994) *Jpn. J. Appl. Phys.*, **33**, 171.

40 Weißmantel, C. and Hamann, C. (1979) *Grundlagen der Festkörperphysik*, Springer, Berlin (in German).

41 Anastassakis, E. (1999) *J. Appl. Phys.*, **86**, 249.

42 Puech, P., Pinel, S., Jasinevicius, R.G., and Pizani, P.S. (2000) *J. Appl. Phys.*, **88**, 4582.

43 Balkanski, M., Wallis, R.F., and Haro, E. (1983) *Phys. Rev. B*, **28**, 1928.

44 Burke, H.H. and Herman, I.P. (1993) *Phys. Rev. B*, **48**, 15016.

45 Verma, P., Abbi, S.C., and Jain, K.P. (1995) *Phys. Rev. B*, **51**, 16660.

46 Raptis, J., Liarokap, E., and Anastassakis, E. (1984) *Appl. Phys. Lett.*, **44**, 125.

47 Pan, M.-W., Benner, R.E., and Smith, L.M. (2002) Continuos lasers for raman spectroscopy, in *Handbook of Vibrational Spectroscopy*, vol. 1, John Wiley & Sons Ltd., Chichester, pp. 490–507.

48 Green, M.A. (1995) *Silicon Solar Cells: Advanced Principles & Practice*, Centre for Photovoltaic Devices and Systems, University of New South Wales, Sidney.

49 Mandelkorn, J. and Lamneck, J.H. (1973) *J. Appl. Phys.*, **44**, 4785.

50 Godlewski, M.P., Baraona, C.R., and Brandhorst, H.W. (1969) Proceedings of the 10th IEEE Photovoltaic Specialists Conference, Palo Alto, p. 40.

51 Gereth, R., Fischer, H., Link, E., Mattes, S., and Pschunder, W. (1972) *Energ. Convers.*, **12**, 103.

52 Huster, F. (2005) Proceedings of the 20th European Photovoltaic Solar Energy Conference and Exhibition, Barcelona, p. 635.

53 Huster, F. (2005) Proceedings of the 20th European Photovoltaic Solar Energy Conference and Exhibition, Barcelona, p. 1462.

54 Huster, F. (2005) Proceedings of the 20th European Photovoltaic Solar Energy Conference and Exhibition, Barcelona, p. 1466.

55 Karg, D., Roy, K., and Koch, W. (2004) Proceedings of the 19th European Photovoltaic Solar Energy Conference, Paris, p. 923.

56 Tochino, S. and Pezzotti, G. (2002) *J. Raman Spectrosc.*, **33**, 709.

57 Pezzotti, G., Okamato, Y., Nishida, T., and Sakai, M. (1996) *Acta Mater.*, **44**, 899.

58 Pezzotti, G. (1999) *J. Raman Spectrosc.*, **30**, 867.

59 Pezzotti, G., Muraki, N., Maeda, N., Satou, K., and Nishida, Y. (1999) *J. Am. Ceram. Soc.*, **82**, 1249.

60 Pezzotti, G., Ichimaru, H., Ferroni, L.P., Hirao, K., and Sbaizero, O. (2001) *J. Am. Ceram. Soc.*, **84**, 1785.

61 Anderson, T.L. (2004) *Fracture Mechanics: Fundamentals and Applications*, Taylor & Francis, London.

62 Hanoka, J.I. and Bell, R.O. (1981) *Ann. Rev. Mater. Sci.*, **11**, 353.

63 Schreck, M., Roll, H., Michler, J., Blank, E., and Stritzker, B. (2000) *J. Appl. Phys.*, **88**, 2456.

64 Herms, M. (2000) *J. Cryst. Growth*, **210**, 172.

65 Wittmann, R., Parzinger, C., and Gerthsen, D. (1998) *Ultramicroscopy*, **70**, 145.

66 Clément, L., Pantel, R., Kwakman, L.F.T., and Rouvière, J.L. (2004) *Appl. Phys. Lett.*, **85**, 651.

67 Ambridge, T. and Faktor, M.M. (1975) *J. Appl. Electrochem.*, **5**, 319.

68 Blood, P. (1986) *Semicond. Sci. Technol.*, **1**, 7.

69 Fano, U. (1961) *Phys. Rev.*, **124**, 1866.

70 Fano, U. (1965) *Phys. Rev.*, **137**, 1364.

71 Fano, U., Pupillu, G., Zannoni, A., and Clark, C.W. (2005) *J. Res. Natl. Inst. Stand. Technol.*, **110**, 583; (Engl. translation of Fano, U. (1935) *Nuovo Cimento*, **12**, 154).

72 Cerdeira, F., Fjeldly, T.A., and Cardona, M. (1973) *Solid State Commun.*, **13**, 325.

73 Cerdeira, F., Fjeldly, T.A., and Cardona, M. (1973) *Phys. Rev. B*, **8**, 4734.

74 Balkanski, M., Jain, K.P., Beserman, R., and Jouanne, M. (1975) *Phys. Rev. B*, **12**, 4328.

75 Watkins, G.D. and Fowler, W.B. (1977) *Phys. Rev. B*, **16**, 4524.

76 Simonian, A.W., Sproul, A.B., Shi, Z., and Gauja, E. (1995) *Phys. Rev. B*, **52**, 5672.

77 Devereaux, T.P. and Hackl, R. (2007) *Rev. Mod. Phys.*, **79**, 175.

78 Klein, M.V. (1983) Electronic Raman scattering, in *Topics in Applied Physics*, vol. 8 (ed. M. Cardona), Springer, Berlin, pp. 147–204.

79 Magidson, V. and Beserman, R. (2002) *Phys. Rev. B*, **66**, 195206.

80 Jouanne, M., Beserman, R., Ipatova, I., and Subashiev, A. (1975) *Solid State Commun.*, **16**, 1047.

81 Chandrasekhar, M., Cardona, M., and Kane, O.E. (1977) *Phys. Rev. B*, **16**, 3579.

82 Chandrasekhar, M., Renucci, J.B., and Cardona, M. (1978) *Phys. Rev. B*, **17**, 1623.

83 Nickel, N.H., Lengsfeld, P., and Sieber, I. (2000) *Phys. Rev. B*, **61**, 15558.

84 Nomarski, G. (1952) French Patents No. 1059124 and 1056361.

85 Miller, D.C. and Rozgony, G.A. (1980) in *Handbook on Semiconductors*, vol. 3 (ed. S.P. Keller), North-Holland Publishing Co. pp. 217–246.

86 Becker, M., Goesele, U., Hofmann, A., and Christiansen, S. (2009) *J. Appl. Phys.*, **106**, 074515.

87 Basore, P.A., Clugston, D.A., Thorson, G., Smith, A., Rover, D., Hansen, B., and Anderson, G. (2003) *Solar Cells Simulation Software*, University of New South Wales, Sidney.

88 Castaign, R., Jouffrey, B., and Slodzian, G. (1960) *Compt. Rend.*, **251**, 1010.

89 Herzog, R.K. and Liebl, H. (1963) *J. Appl. Phys.*, **34**, 2893.

90 Benninghoven, A. (1970) *Z. Phys.*, **230**, 403.

91 Schroder, D.K., *Semiconductor Material and Device Characterization*, 2nd edn, John Wiley & Sons, Inc., New York, pp. 683–689.

92 Schulze, H.J., Lüdge, A., and Riemann, H. (1998) *J. Electrochem. Soc.*, **143**, 4105.

93 Rauch, T., Böberl, M., Tedde, S.F., Fürst, J., Kovalenko, M.V., Hesser, G., Lemmer, U., Heiss, W., and Hayden, O. (2009) *Nat. Photon.*, **3**, 332.